Slow light in photonic crystal waveguides for reinforced interaction with matter

Xiaorun Zang

université de BORDEAUX

THÈSE PRÉSENTÉE

POUR OBTENIR LE GRADE DE

DOCTEUR DE
L'UNIVERSITÉ DE BORDEAUX

ÉCOLE DOCTORALE EN SCIENCES POUR L'INGENIEUR (SPI)

SPÉCIALITÉ: LASERS, MATIERES, NANOSCIENCES

Par Xiaorun ZANG

Slow Light in Photonic Crystal Waveguides for Reinforced Interaction with Matter

Sous la direction de : Philippe LALANNE

Soutenue le 29 Septembre 2015

Membres du jury :

M. DE WILDE, Yannick	Directeur de Recherche	Institut LANGEVIN, ESPCI	Président
M. FELBACQ, Didier	Professeur	Université Montpellier II	Rapporteur
M. DE ROSSI, Alfredo	Researcher	Thales Group	Rapporteur
M. DUTIER, Gabriel	Associate Professor	Université Paris 13	Examinateur
M. LALANNE, Philippe	Directeur de Recherche	Université de Bordeaux	Directeur de thèse

Titre : Lumière lente dans les guides à cristaux photoniques pour l'interaction renforcée avec la matière

Résumé : Dans cette thèse, nous avons étudié l'impact considérable de désordre aléatoire sur le transport de la lumière lente dans les guides à cristaux photoniques 1D, c'est-à-dire la localisation de la lumière. Les mesures en champ proche, les simulations statistiques et le modèle théorique révèlent l'existence d'une limite inférieure de l'extension spatiale des modes localisés. Nous avons également présenté que le niveau de désordre et l'extension spatiale de mode localisé individuelle sont liés par la masse effective de photons plutôt que la vitesse de groupe considérant en général.

Deuxièmement, les systèmes hybrides d'atomes froids et des guides à cristaux photoniques ont été reconnus comme un approche prometteuse pour l'ingénierie grande interaction lumière-matière au niveau des atomes et des photons individuels. Dans cette thèse, nous avons étudié la physique, à savoir le transport de la lumière dans des guides de nanophotonique périodiques couplées à des atomes à deux niveaux. Notre expression semi-analytique développée est générale et peut rapidement caractériser le couplage entre les atomes froids et les photons guidées. Pour surmonter les difficultés techniques considérables existent dans les systèmes hybrides atomique et photonique, nous avons conçu un guide nanophotonique qui supporte un mode de Bloch lente guidée avec grande queue évanescente dans l'espace libre pour les atomes froids de piégeage. Pour adapter précisément la région de fréquence de la lumière lente du mode guidé à la ligne de transition atomique, nous avons conçu la bande photonique et de la courbe de dispersion du mode guidé afin que la force de l'interaction est robuste contre imprévisible fabrication imperfection.

Mots clés : lumière lente, localisation de la lumière, des guides à cristaux photoniques, l'interaction atome-photon, Bloch l'expansion des modes.

Title: Slow Light in Photonic Crystal Waveguides for Reinforced Interaction with Matter

Abstract : In this thesis, we firstly investigated the striking influence of random disorder on light transport near band edges in one dimensional photonic crystal waveguides, i.e. light localization. Near-field measurements, statistical simulations and theoretical model revealed the existence of a lower bound for the spatial extent of localized modes. We also showed that the disorder level and the spatial extent of individual localized mode is linked by the photon effective mass rather than the generally considered group velocity. Secondly, hybrid cold atoms and photonic crystal waveguides system have been recognized as a promising paradigm for engineering large light-matter interaction at single atoms and photons level. In this thesis, we studied the basic physics, i.e. light transport in periodic nanophotonic waveguides coupled to two-level atoms. Our developed general semi-analytical expression can quickly characterize the coupling between cold atoms and guided photons. Aim to overcome the significant technical challenges existed for developing hybrid atom-photonic systems, we designed a nanophotonic waveguide, which supports a slow guided Bloch mode with large evanescent tail in free space for cold atoms trapping (release the limitation imposed by Casmir Polder force and technical challenge of nanoscale manipulation of cold atoms). To match precisely the slow light region of the guided mode to the atomic transition line, we carefully engineered the photonic band and the dispersion curve (i.e. flatness) of the guided mode so that the interaction strength is robust against unpredictable fabrication imperfection.

Keywords : slow light, light localization, photonic crystal waveguide, atom-photon interaction, Bloch modes expansion.

Unité de recherche

[Laboratoire Photonique, Numérique et Nanosciences (LP2N), UMR5298, Rue F. Mitterrand 33400 TALENCE cedex, France]

Résumé en français

Le traitement tout optique du signal est une technique prometteuse qui peut offrir de meilleures performances pour les réseaux d'information de prochaine génération, car elle évite la faible efficacité de la conversion optique-électronique aux nœuds de réseaux d'information. La lumière lente dans des guides de cristaux photoniques peut stimuler non-linéarité optique, donc il offre des possibilités sans précédent pour la réalisation de traitement tout optique du signal. Dans ce travail de recherche, nous nous concentrons sur deux phénomènes dans les dispositifs à cristaux photoniques avec lumière lente : 1) la localisation de la lumière dans les guides à cristaux photoniques avec le désordre ; 2) la grande interaction lumière-matière dans les systèmes hybrides du quantum et de guides à cristaux photoniques. Ce qui suit est un bref résumé de ma thèse.

Dans le chapitre 2, nous allons étudier l'influence du désordre sur le transport de la mode guidé lente à cristaux photoniques. Comme nous le savons tous, les imperfections de fabrication sont inévitables dans des dispositifs réels de silicium photonique. Les études initiales montrent que les imperfections de fabrication ont des impacts importants sur le transport de la lumière lente, en particulier à des fréquences proches de la limite de la bande. L'impact le plus évident est sans doute la formation de modes localisés au voisinage de bande interdite photonique. La localisation de la lumière dans les guides à cristaux photoniques a attiré spécialement en raison des limites importantes qu'il impose à la réalisation de dispositifs photoniques avec la lumière lente. Nous démontrons l'existence d'une limite inférieure de la taille de mode, c'est-à-dire que les modes localisés ne peuvent pas être inférieur à un certain seuil de taille dans une structure photonique donnée pour un niveau de désordre donné. En outre, nous présentons ce que la limite est reliée à la masse efficace de photons (la courbure de la courbe de dispersion) plutôt que l'index de groupe.

Les mesures en champ proche sur des guides à cristaux photoniques et des calculs numériques sur diverses structures montrent sans équivoque que les médias périodiques avec les courbes de dispersion plats peuvent naturellement former étonnamment-petits (échelle de longueur d'onde) modes localisés. Une loi d'échelle est proposée pour décrire le rôle de la masse effective du photon en le confinement de la lumière, et il se trouve à être en accord avec les résultats expérimentaux et numériques.

Nos résultats pourraient être instructif pour la conception des dispositifs photoniques dans lesquels le désordre devient une limitation stricte sur les fonctionnalités des dispositifs photoniques. Par exemple, la localisation de la lumière peut être mieux exploitée pour améliorer les performances du dispositif d'applications dans l'imagerie biologique, l'effet du laser aléatoire et l'énergie solaire. D'autre part, pour des applications dans les systèmes hybrides d'atomes froids et de la nanophotonique où la localisation de la lumière potentiellement altère la fonctionnalité des systèmes, même avec la technologie de fabrication state-of-the-art, la localisation induite par le désordre doit être soigneusement évitée. En tout cas, nous espérons que notre étude bénéficiera les conceptions ultérieures avec de haute performance et de robustesse. Du point de vue de la physique fondamentale, notre accent sur la courbure de la courbe de dispersion, à savoir la masse effective du photon, peut inspirer la compréhension conceptuelle de la localisation d'Anderson dans des milieux désordonnés.

Dans le chapitre 3, nous proposons un traitement théorique de l'interaction entre les atomes à deux niveaux et des guides d'ondes périodiques. La grande interaction lumière-matière joue un rôle essentiel dans la réalisation du « on-chip-processing » optiques. Les nanostructures de lumière lente sont systématiquement utilisées pour améliorer les interactions lumière-matière en modifiant la densité d'états locale de photons virtuels. Récemment, les nouveaux systèmes hybrides quantiques-- combinant atomes ultra-froids et dispositifs nanostructurés--ont émergé. La combinaison des excellentes propriétés de cohérence des systèmes quantiques avec une plate-forme très flexible pour la mise en œuvre de fortes interactions à l'échelle sous-longueur d'onde est prévu de dépasser des paramètres classiques de l'électrodynamique quantique des l'état solide avec les points quantiques. Les exemples comprennent des fibres optiques ultra-fines, des cavités à cristaux photoniques formés à partir de matériaux diélectriques planes, et, plus récemment, des guides périodiques à cristaux photoniques, pour lesquels la forte amélioration du champ au bord de la bande porte un potentiel élevé pour l'interaction atome-photon.

La physique essentielle de traitement tout optique du signal quantique avec les guides périodiques est la diffusion de photons guidés par des atomes piégés à proximité du guide d'ondes, qui est caractérisé par la matrice de diffusion d'un atome. Le principal défi pour le calcul de la matrice de diffusion découle de l'évaluation de la décroissance de l'émission dans les modes de rayonnement. Parce qu'il faut mettre en œuvre les conditions précises d’onde sortant dans les directions périodiques. Bien que les limites absorbantes (les couches parfaitement appariés) ont été récemment optimisée, toute résiliation qui rompt la périodicité et

les calculs numériques reposant sur un échantillonnage 3D sont inévitablement contaminés par la résiliation rétrodiffusion, en particulier pour les petites vitesses de groupe. Nous surmontons le problème en utilisant une approche qui ne dépend pas le maillage numérique dans les directions périodiques mais plutôt sur une expansion analytique dans le Bloch quasi-normale modes base. L'approche offre l'avantage de proposer pratiquement prédictions exactes pour le taux de désintégration spontanée totale, mais cependant il repose sur des outils numériques avancés rares et sur les calculs qui doivent être répétées pour chaque position de l'atome. Ainsi, il est avantageux d'envisager un traitement d'approximation, dans lequel le taux de désintégration spontanée dans tous les autres modes de Bloch est supposé être égal à (ou un facteur constant multiplie) le taux d'émission dans le vide. L'approche de l'expansion des modes de Bloch quasi-normales avec le traitement d'approximation ci-dessus, nous permettent de prédire analytiquement la réponse spectrale pour chaque fréquence, pour tout l'intensité du champ (dans la région de couplage faible) et pour tout l'emplacement de l'atome. La prédiction nécessite seulement la connaissance de la distribution du champ électrique motrice, qui est facile à calculer pour les structures diélectriques et métalliques avec solveurs Bloch-mode. Les expressions sont généralement valables pour les deux guides d'ondes photoniques et plasmoniques, et la seule restriction étant que le matériau de guide d'ondes soit réciproque. Parallèlement, l'expression analytique est pratique car elle offre une compréhension en profondeur et permet un calcul très efficace des réponses optiques lorsque certains paramètres physiques sont modifiés, telles que la vitesse de groupe ou la position d'atome. La matrice de diffusion développée ici est valable pour interaction lumière-matière dans la région de couplage faible, mais ce résultat général ne se limite pas à notre géométrie de guide d'onde spécifique.

Dans le domaine émergent de l'intégration de dispositifs nanophotonique et les atomes froids, Il existe, en effet, de nombreuses difficultés en dépit de l'impact profond sur le traitement tout-optique et l'informatique quantique qu’il peut apporter. Les défis comprennent le chargement de l'atome, la diffusion de la lumière des imperfections dans les dispositifs, l'appariement des résonances atome-phonons, etc. Dans le chapitre 4, nous concevons un nouveau géométrique qui offre une forte interaction entre les atomes et la lumière lente pour les atomes qui sont dans le vide à une distance quart d'onde du guide d'onde. Dans le contexte de la forte interaction lumière-matière, un obstacle depuis longtemps est de réaliser une forte interaction entre les atomes et des photons uniques, tout en assurant en même temps le piégeage des atomes dans le vide à de grandes distances de séparation des surfaces diélectriques. En général, la lumière lente est une conséquence de champs de mode coopérant avec une structure périodique. Le ralentissement

efficace de la lumière peut être réalisé lorsque le champ de mode se propage dans un canal ondulé; Toutefois, il est en contradiction avec l'objectif de mettre en œuvre des bandes de dispersion plats avec un champ de mode qui réside principalement dans le vide où les atomes sont chargés. La conception actuelle qui utilise la lumière lente dans des guides d'ondes à cristaux photoniques est ne certainement pas optimale, mais il offre l'avantage de présenter directement le conflit et d'offrir une solution de compromis. En outre, en ce qui concerne le piégeage des atomes froids, il découple le piégeage des atomes froids et de l'interaction atome-photon et offre un accès 2π angle solide de la région d'interaction, qui permet des manipulations "faciles" de nuages atomiques autour de la structure par d'autres ondes stationnaires externes. Enfin, la courbe de dispersion d'ingénierie du guide proposé (car il possède de grandes masses efficaces de photons en comparaison avec les travaux antérieurs) offre un design robuste et nous permet d'adapter précisément la transition atomique et les fréquences de lumière lente.

Dans le chapitre 5, nous avons étudié la performance de la convergence des outils numériques qui a été utilisée dans la thèse pour prédire certaines qualités essentielles caractérisant l'interaction atome-champ. En outre, les techniques numériques décrites dans ce chapitre, par exemple, l'approche de normalisation, peuvent être utile dans la pratique pour les études théoriques des interactions lumière-matière dans les systèmes hybrides d'atomes froids et la nanophotonique.

Acknowledgements

First and foremost, I would like to express my sincere gratitude to my supervisor, Professor Philippe LALANNE, for giving me the opportunity to finish my PhD in a hot research area. Without his acceptance, my three years' PhD study would not even start.

It was a shame that I did not have solid background on optics and nanophotonics at the beginning of my PhD. It is still clear in my mind that my supervisor spent almost half of his day with me in the first half year which is really appreciable. At the beginning, I didn't know how to use our in-house Matlab package to do simulations. But, Philippe spent time to make word instructions particularly for me. What's more, he sometimes debugged program with me. Working with him, I have learned how to question critically, how to be precise in a report, etc. professional qualifications that are necessities in future research career.

Maybe the culture between France and China is quite different and sometimes Philippe felt difficult to communicate with me. But he admitted this difference and has always tried to improve the efficiency of our discussions. Also, another Chinese postdoc, Jianji Yang, has helped me a lot to master the spirit of Philippe's idea.

Also, I would like to thank my colleagues, Kevin and Rémi, for the fruit discussions with them. Rémi is quite self-motivated than me and he has strong questioning spirit which are excellent qualities that influence me a lot. Kevin was always smiling and was always patient with my questions and requests. Kevin even helped me on French emails to communicate with my previous landlord when I had trouble to live in my previous apartment. I also want to take this opportunity to thank the laboratory administration for providing all the necessary facilities for the research.

In addition, I would like to thank my parents and my elder brother for their full support. My parents missed so much, but I could only come back to see them once a year. I would like to say sorry to my parents.

During my PhD study, my girlfriend has accommodated herself to my life style especially for someday when I had to work late until midnight. I do appreciate that her understanding of my work and her kind encouragement when I was trapped either in my research or in my life.

At last, this research gets financial support from Université de Bordeaux.

Contents

List of Figures

1 Introduction

In modern information networks, digital data is sent and received through optical fibers as photons over long-distance. Undoubtedly, the massive and low-cost production of low-loss optical fibers has greatly advanced the data transmission rate in information communication. All-optical information processing, e.g. all-optical switching, routing or modulating, is a promising technique that may offer higher performance for next-generation information networks since it avoids the low efficient optical–electronic conversion at network nodes [Bab08; Sol04]. Photonic crystal devices implementing slow light effect can boost optical nonlinearity that is required for all-optical processing [Sol04], thus it provides unprecedented opportunities for realizing all-optical information processing.

In this thesis, we focus on two phenomena involve in slow light photonic crystal devices: 1) light localization in disordered photonic crystal waveguides; 2) strong light-matter interaction in hybrid quantum and photonic crystal waveguides systems. The outline of the chapters is as follow.

In chapter 2, we will investigate the influence of disorder on slow light transport in photonic crystal waveguide.

As we know, fabrication imperfections are unavoidable in any real silicon-photonic devices. Initial studies show that fabrication imperfections have significant impacts on slow light transport, especially at frequencies close to the band edge [Not01; Vla99]. The most striking impact is undoubtedly the formation of localized modes in the vicinity of photonic band gaps [Joh91].

Localization in photonic crystal waveguides has garnered special attention due to the important limitations it imposes on the realization of slow light photonic devices [Not01; Boy11; Mel14; Hug05a; Maz09]. We demonstrate the existence of a lower bound in the mode size, i.e. the localized modes cannot be smaller than a certain size threshold in a given photonic structure for a given disorder level. In addition we show that the bound is related to the effective photon mass (the curvature of the dispersion curve) rather than the group index. In Fig. 1-1, we schematically illustrate the light localization at a band edge, which comes from both sides of the gap.

Near-field measurements on photonic crystal waveguides and numerical calculations on various structures unambiguously show that periodic media with flat dispersion curves can naturally form surprisingly-small (wavelength scale) localized modes. A scaling law is proposed to describe the role of the effective photon mass on light confinement and is found to be in agreement with experimental and numerical results. We believe that this new physical understanding on light localization near band edges not only constitutes an important conceptual advance on the topic, but could also impact future photonic device designs by offering the possibility to either reduce or enhance the effect of tiny perturbations on light propagation and confinement.

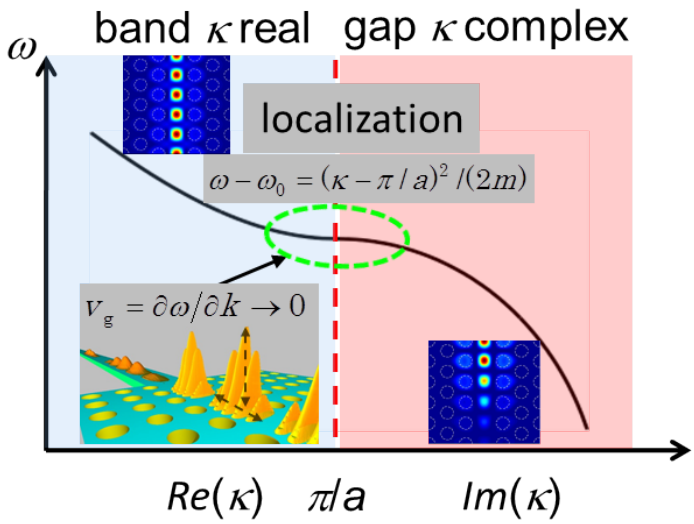

Fig. 1-1. Light localization in the vicinity of photonic band gaps encircled by the green dash ellipse. In the band diagram, the left blue region represents the pass band (supporting a propagating Bloch mode) while the right red region represents the band gap (which supports evanescent Bloch modes only), slow light happens as the group velocity v_g tends to 0. The dispersion curve close to the band edge cutoff is approximated by a quadratic expression in which ω and ω_0 are the operation and the cutoff frequencies, κ is the complex wave vector, a is the lattice constant, m is the photon effective mass that implies the curvature of the dispersion curve.

In chapter 3, we propose a theoretical treatment of the interaction between two-level atoms and periodic waveguides.

Strong light-matter interaction plays a pivotal role in the realization of on-chip optical information processing. Slow-light nanostructures are routinely used to enhance light-matter interactions by modifying the local density of virtual photon states. Recently, new hybrid quantum systems -combining ultracold atoms and nanostructured devices- have emerged. The combination of excellent quantum coherence properties with a very flexible platform for implementing strong interactions at subwavelength scales is expected to go beyond classical settings of all-solid-state QED with quantum dots [Lod15]. Examples include ultra-thin unclad optical fibers [Kie04; Kie05; War07], photonic-crystal cavities formed from planar dielectrics [Tho13], and more recently photonic periodic waveguides, for which the strong field enhancement at the band edge bears a high potential for atom-photon interaction [Gob14; Yu14; Gob15]. Behind all-optical quantum information processing with periodic waveguides, the essential physics is the scattering of guided photons by trapped atoms near the waveguide, which is characterized by the scattering matrix of one atom, as illustrated by Fig. 1-2.

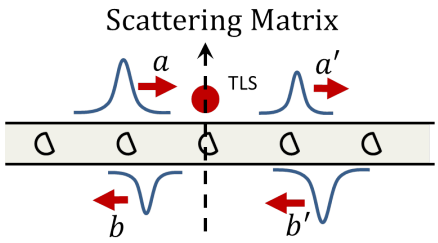

Fig. 1-2. Light scattering property of a single atom in a periodic waveguide that is fully characterized by the scattering matrix S. The red solid point represents two level system (TLS). The incident waves are denoted by letters a and b', the outgoing waves are a' and b.

The scattering-matrix derivation is based on a combination of electromagnetic Bloch-mode-expansion techniques with the optical Bloch equations. The former provides an accurate electromagnetic description of the system, including the local electric field and local density of electromagnetic states, and the latter allows us to describe the population evolution of the quantum system, assumed to be a two-level system. The derivation is inspired from earlier theoretical works on the coupling of quantum emitters with translation-invariant dielectric [She05; Koj03; Man07] or metallic [Cha07; Gon11] waveguides, and coupled-resonator guides [Zho08; Cha11].

The main challenge for calculating the scattering matrix arises from the evaluation of the emission decay into radiation modes. Because it requires implementing accurate outgoing wave conditions in the periodic directions. Although PML-like absorbing boundaries in periodic media have been recently optimized, any termination breaks periodicity and numerical calculations relying on a 3D sampling is inevitably contaminated by termination backscattering, especially for small group velocities. We overcame the issue by using an approach that does not rely on numerical meshing in the periodic directions, but rather on an analytical expansion in the quasi-normal Bloch modes basis. The approach provides the advantage to propose virtually "exact" predictions for total spontaneous decay rate, but in turn it relies on uncommon advanced numerical tools and on calculations that need to be repeated for every atom position. Thus it is advantageous to consider an approximate treatment, in which the spontaneous decay rate into all the other Bloch modes is assumed to be equal to (or a constant factor times) the emission rate in vacuum. The quasi-normal Bloch modes expansion approach together with the above approximate treatment, allow us to analytically predict the spectral response for any driving frequency, field intensity (in weak coupling region) and atom location. The prediction only requires the knowledge of the driving electrical-field distribution, which is easily calculated for dielectric or metallic structures with Bloch-mode solvers.

Several implications of the scattering matrix are obtained. Firstly, the transmission coefficients for two counter propagating Bloch modes are identical; Secondly, one cannot overlook the phase difference between the reflection coefficients related two counter propagating modes; Thirdly, the reflectance of two counter propagating modes are equal for non-absorbent dielectric waveguides while different for the metallic waveguides. Lastly, at low power of the incident guided mode, the saturation term is dropped and the atomic response spectral is determined by the total decay rate and as the band edge is tuned to the atomic transition line, the total decay rate is mainly driven by the coupling to the waveguide mode thus

proportional to the group index.

The expressions are generally valid for both photonic and plasmonic waveguides, the only restriction being that the waveguide material be reciprocal. At the same time, the analytical expression is comfortable in practice since it favors an in-depth understanding and allows a very efficient computation of the optical responses when some physical parameters are modified, such as the group velocity or the atom position. The scattering matrix developed here is valid for light-matter interaction in weak coupling region, but this general result is not restricted to our specific waveguide geometry.

In chapter 4, we design a novel geometric which offers strong interaction between atoms and slow light for atoms that are place in vacuum at quarter-wavelength distance from the waveguide.

In the context of strong light-matter interaction, a long-standing obstacle is to achieve strong interaction between single atoms and single photons, while at the same time trap atoms in vacuum at large separation distances from dielectric surfaces. In general, slow light is a consequence of mode fields interacting with a periodic structure. Efficient light slowdown can be achieved when the mode field propagates inside a corrugated channel medium; however, this fact conflicts with the desire for implementing flat dispersion bands with a mode field that dominantly resides in the vacuum cladding where the atoms are loaded. The present design (shown in Fig. 1-3) that uses slow-light in photonic crystal waveguides is certainly not optimal, but it offers the benefit to directly address the conflict and to present a compromised solution.

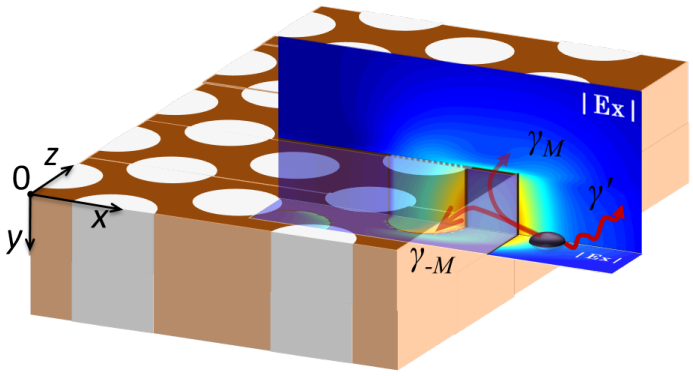

Fig. 1-3. Interaction between atoms and slow light. The modal profile is the *x*-component of the electric field of the slow light Bloch mode. The purple ellipsoid represents the cold atom trapped in the vicinity of the photonic crystal waveguide where it still feels a strong evanescent field of the guided Bloch mode. Its coupling coefficients into the forward- and backward-propagating mode are γ_{M} and $\gamma_{-\mathrm{M}}$ separately, left the γ' accounting the coupling into all the other modes.

The current slow-light approaches [Gob14; Yu14; Dou15] involve the combination of two frequencies operations, i.e. one for trapping and one for probing, which represents not only a technical but a design challenge. In addition, the atom is loaded into a narrow slot of 250 nm wide where the inevitable interactions with the surface can alter the trap potential and even cause heating and loss of trapped atoms. We propose a hybrid-clad waveguide in which we

decouple the trapping and atom-field-interaction problems. Geometrically, the hybrid-clad waveguide offers a 2π solid-angle access to the interaction region, allowing for easy manipulations of cold atomic clouds around the structure.

From the fabrication point of view, the devices robustness against fabrication imperfection must be taken into account. Since one of the two key factors determining the strength of light-matter interaction is group velocity, we consider how the devices group velocity evolves as the disorder level varies. We use a power-series to expand the dispersion curve at the atomic transition frequency to analyze the evolution of the group velocity as a function of disorder level. We find the flat dispersion curve (large effective photon mass) of the guided Bloch mode implies that the design is robust in terms of imperfection tolerance in fabrication process.

In the chapter 5, as a complement we will detail the numerical simulations performed in chapter 3 and 4 and we also check the accuracies of our numerical results therein so that our discussions and conclusions are valid.

2 Wavelength-scale localization with heavy photons

In this chapter, we are concerned by light localization in disordered photonic crystal waveguides with flat dispersion bands ("heavy photons", the definition of effective photon mass is given in section 2.3). We will begin with a brief historical review of Anderson localization, especially of light localization in photonic crystal waveguide. In section 2.2, we provide experimental and numerical results that evidence the formation of wavelength-scale localized modes at the band-edge of photonic structures at very small disorder levels. As we will describe in section 2.3, the formation of localized modes at the band-edge rely on an intricate interplay between multiple scattering of propagating waves, which gives rise to Anderson localization, and evanescent damping due to the photonic band-gap (also refer the schematic diagram Fig. 2-1 in section 2.1). To understand the physical mechanism underlying the formation of localized modes, in section 2.3 we also propose a scaling law that relates the disorder level to the modes spatial extent which reveals that such modes naturally form up in PhCWs at intrinsic disorder levels due to the flatness of the dispersion curve. Readers interested in details on the statistical computations can refer to section 2.4. Finally, we will end with conclusions and perspectives.

2.1 Introduction

Localization phenomenon was initially studied by Nevill Francis Mott [Mot49] and Philip Warren Anderson [And58] in their pioneering work of metal-insulator transition , i.e. electrons transport goes from diffusion into localization in disordered solids. For Mott localization, strong repulsive Coulomb interaction screens the electrons from diffusing so that electronic localization happens. In Anderson localization, however, the absence of diffusion results from interference of all the scattered electronic waves. As it is a universal wave phenomenon, Anderson localization has also been studied for other types of waves, e.g. microwaves [Dal91], sound waves [Wea90] and Bose-Einstein condensates [Bil08; Roa08] and electromagnetic waves as well [Joh84; And85]. One of the advantages in optical systems is that the photons do not interaction with one another, in contrast to electronic systems for which electron-electron interactions and electron-phonon scattering hinders the observation of Anderson localization in disordered solids. However, the formation of 3D Anderson localization is very challenging since strong multiple scattering is difficult to achieve [Joh87; Lag09]. Some recent reports on Anderson localization in strongly scattering powders of gallium arsenide [Wie97] and titanium dioxide [Stö06; Spe13] was questioned since all the works cannot exclude the influence of fluorescence and nonlinearity [Wie13]. To reduce the difficult of observing Anderson localization, one possibility is to diminish the dimensionality of the system. One example of lower-dimensional system is photonic crystal waveguide that may possesses a photonic crystal bandgap [Yab87]. In photonic crystal waveguide structure, since light transport is inhibited in certain directions, light localization is easier even for moderate disorder [Joh87].

In this chapter, we are concerned by localization of light in photonic crystal waveguide (PhCW). If the waveguide is monomode and if we neglect out-of-plane loss, the system is one dimensional (1D) and any disorder level (even extremely small) leads to Anderson localization, provided that the waveguide length is longer than the localization length [Moo08].

Initially, research on light transport in PhCW have been undertaken for silicon-photonic applications, the influence of disorder (fabrication imperfections) becomes significant from the initial studies on slow light transport, especially at frequencies close to the band edge [Not01; Vla99]. Rapidly, it was then realized that fabrication imperfections drastically impact the back reflection that scales as n_g [Maz09], favoring formation of Anderson localization, at the expense of the light transport. Thus, from initial applied perspectives in silicon photonic, the topic has recently involved into more fundamental questions [Bar11; Sap10; Hui12].

Our present understanding of light localization in periodic photonic crystal waveguide is summarized in Fig. 2-1. The solid blue and red curves represent the dispersion relation of a Bloch mode in a perfectly periodic PhCW. On the left side in the pass band (blue segment of the dispersion curve), the Bloch mode supported by the structure is guided with a real propagation constant κ $(Im(\kappa) = 0)$. On the right side in the band gap (red segment of the dispersion curve), the Bloch mode is an evanescent gap mode with a complex κ and $Re(\kappa) = \pi/a$.

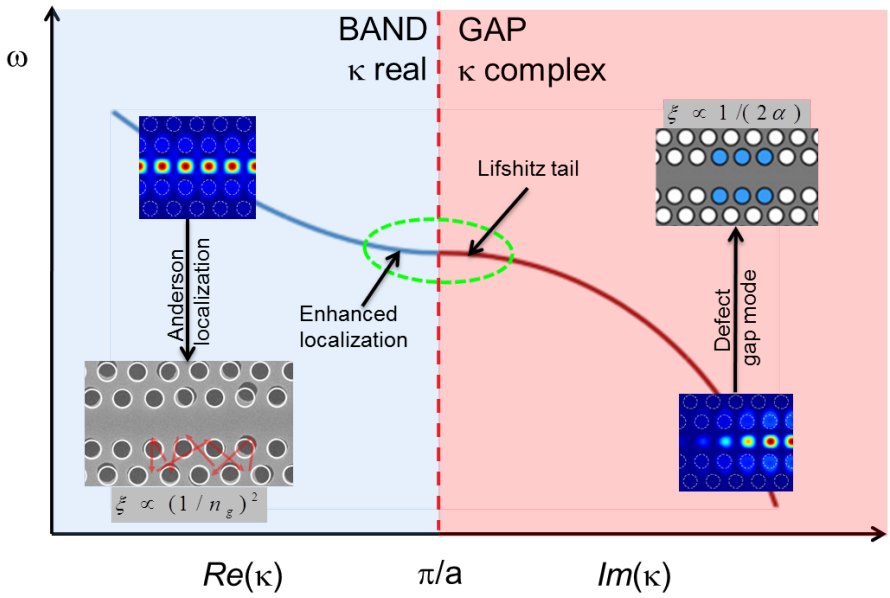

Fig. 2-1. The formation of localized modes. It consists of two regions, i.e. the pass band on the left side (light blue) and the band gap on the right (light red). The solid curve represents the dispersion relation of a Bloch mode in a perfectly periodic PhCW. In the pass band (blue segment of the dispersion curve), the Bloch mode supported by the structure is guided with a real propagation constant κ $(Im(\kappa) = 0)$. In the band gap (red segment of the dispersion curve), the Bloch mode is an evanescent gap mode with a complex κ and $Re(\kappa) = \pi/a$. In the presence of moderate disorder, the multiple scattering in the pass band forms the light localization of Anderson type with its localization length varies as $(1/n_g)^2$. While, in the band gap the evanescent decay results in the light localization of cavity type, with the attenuation length scales as $1/(2\alpha)$. The dashed green ellipse encloses the enhance localization regime and the photonic Lifshitz tail.

In the presence of a slight disorder, light transport is altered. As shown in Fig. 2-1, deep in the band gap, localization is due to a confinement by evanescent modes. The localized modes

are in many aspects similar to the defect modes of engineered nanocavities, in analogy to the Mott localization of electrons in disordered solids. The localization length coincides with the band gap attenuation length, which is simply related to the imaginary part α of the Bloch wavevector as $\xi = 1/(2\alpha)$. At frequencies above the band edge, disorder gives rise to multiple scattering and constructive interference results in Anderson localization. As frequency ω is reduced and one approaches to the band edge, the group velocity of the Bloch mode is reduced and the impact of disorder is enhanced. Many experimental and theoretical works have shown that the localization length scales as $\left(1/n_{\mathrm{g}}\right)^2$ [Pat09; Maz09]. Finally, for the sake of completeness, let us mention that localized modes at frequencies just smaller than the band edge have been observed [Hui12]. These modes formed in the photonic Lifshitz tail are understood as the analogue of the gap modes but at higher frequencies.

To date, a comprehensive description of the physical mechanisms underlying the relation between the disorder level and the spatial extent of localized modes formed at the band-edge is still missing. The lack of understanding is critical especially for small (wavelength-scale) localized modes that enhance the interaction of light with matter, and for very small disorder levels ($\sigma < \lambda/1000$) that are inevitably left by the imperfections of any fabrication technology and yet can dramatically impact light propagation and trapping [Joh87; Tag11]. Finding out how small a localized mode can possibly be for a given small disorder level and on what structural characteristics this minimal size depends would bring deeper knowledge into the physics of light localization at band-edges of periodic media and may impact the design of future devices.

In this chapter, we investigate the formation of localized modes in 1D randomly-perturbed optical periodic media near the photonic band-edge. While the group index is generally considered to be the key quantity in this process, we demonstrate that the relation between the disorder level and the spatial extent of individual localized modes is driven instead by the continuous quantity effective photon mass, i.e. the second derivative $\partial^2\omega/\partial k^2$. In this mixed regime close to the band edge, the physical mechanisms responsible for localization results from an intricate interplay between multiple scattering and band gap attenuation. Near-field measurements on photonic crystal waveguides and statistical numerical calculations on various structures reveal that periodic media exhibiting flat dispersion bands can support surprisingly small localized modes at almost imperceptible disorder levels ($\sigma < \lambda/1000$). A scaling law that relates the disorder level to the modes spatial extent is proposed and is found to agree well with the numerical and experimental results.

2.2 Formation of localized modes

Hereafter, we investigate the formation of wavelength-scale localized modes at the band-edge of photonic structures at very small disorder levels. This work has been done in collaboration with Thomas F. Krauss, Sebastien A. Schulz and Bryan O'Regan at University of St Andrews in UK and Frédérique de Fornel , Benoît Cluzel and Loïc Lalouat at Université de Bourgogne in France. In contrast with the widely-held view that the key quantity impacting localization near band-edges is the group index, we argue that the relation between the disorder level and the mode spatial extent is driven by the effective photon mass. Near-field measurements on PhCWs fabricated without any intentional disorder reveal a surprisingly small localized mode. The observation is supported by extensive numerical simulations, which unambiguously show that only periodic media with flat dispersion bands ("heavy photons") are

capable of forming very small localized modes at very small disorder levels ($\sigma < \lambda/1000$). Based on a Fabry-Perot-like picture, we propose a scaling law relating the disorder level to the mode spatial extent via the effective photon mass, and explain how wavelength-scale localized modes are formed at vanishingly-small disorder levels.

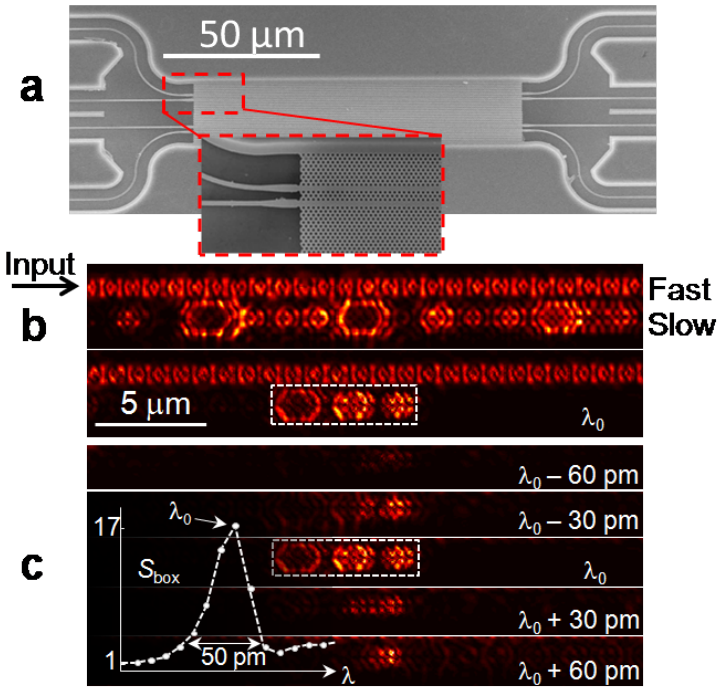

Fig. 2-2. Experimental observation of wavelength-scale localized mode. (a) Scanning electron microscope image pictures of the sample. The inset provides a close-up of the two side-coupled 84-µm-long waveguides, a slow W1 (top) and a fast W1.1 (bottom), and of the access ridge waveguides used to inject light. (b) High-resolution (10 pm) near-field images of the PhCW doublet recorded over an area covering the first 25 µm of the PhCWs. In each image, the top regular pattern corresponds to the fast W1.1 PhCW and localized features are located in the slow W1 PhCW underneath. The top panel shows an extended state (λ_0 = 1489.61 nm) composed of a series of coupled cavities. The bottom panel shows a wavelength-scale mode (λ_0 = 1488.38 nm) composed of three subspots. (c) Spectral evolution of the wavelength-scale mode. The left inset shows the intensity Sbox(λ) integrated over the rectangular dashed-line box and normalized to the averaged intensity in the W1.1 waveguide.

2.2.1 Near-field experiment

To study the formation of wavelength-scale modes in the vicinity of the photonic band-edge at vanishingly small disorders, our collaborators at University of St Andrews in UK fabricate single-row-missing (W1) PhCWs without adding any intentional disorder during the writing process, so that the sole perturbation that remains is the inevitable residual disorder caused by our state-of-the-art fabrication technology. The typical disorder level of the fabrication facility has been characterized by thorough statistical analysis in prior studies and was found to be $\sigma \sim$ 1-2 nm ($\sim$ 0.001λ) [Por11]. Though the procedure lacks control compared to previous studies

that introduce intentional random perturbations [Top07; Sap10; Thy12], we are able to reach a minute and unprecedented level of perturbation that has never been probed up to now near photonic band-edges. An high-resolution scanning electron microscope(SEM) micrograph of a typical set of waveguides fabricated into a 220-nm thick free-standing silicon membrane is shown in Fig. 2-2(a). The hexagonal lattice constant is a = 420 nm and the hole radius is $0.3a$. At vanishingly small group velocities, the optical mean free-path is very short and coupling light into localized modes cannot be achieved by end-fire injection through cleaved facets [Top07]. For this reason, the layout consists of a pair of collinear waveguides: a W1 waveguide operating in the slow-light regime near the band-edge wavelength $\lambda_c \sim$ 1490 nm, and a W1.1 (10% larger defect-width) waveguide operating in the fast-light regime. The latter can then be used as an independent channel for delivering light into the localized modes supported by the former.

Because of their small spatial extensions and spectral bandwidths, wavelength-scale modes localized by disorder are challenging to observe. Therefore, for a rapid initial exploration over broad spatial and spectral intervals, our collaborators at Université de Bourgogne in France first use low-spectral (200 pm) and low-spatial resolution (100 nm) multispectral near-field scanning-optical microscopy (SNOM) using a tapered monomode silica fiber probe and a supercontinuum laser source [Del12]. Due to the lack of spectral resolution, the images recorded in the 1480–1500 nm band cannot reveal localized modes with a quality factor Q > 10,000. They distinguish two types of states for wavelengths close to the W1 PhCW cut-off at 1487 nm. The most frequent ones are delocalized states that extend over most of the scanned area and exhibit numerous spatial bright spots. More interesting in the present context is the existence of less probable, wavelength-scale localized modes; two modes at λ = 1488.3 or 1491.5 nm. With high-resolution SEM analysis of the W1 waveguide, they have checked that those modes are not due to abnormally large, albeit inevitable, fabrication local defects (see Fig. 2-3), but rather to the residual intrinsic imperfections inherent to the fabrication process over the entire waveguide structure. This conjecture is later confirmed by computational results.

For a deeper analysis, our collaborators at Université de Bourgogne resort to high spectral-resolution SNOM with a 1-pm-resolution tunable laser, increasing the spatial sampling to ~ 62 nm and scanning the W1 waveguide at spatial locations found with low resolution. This allows us to detect modes with larger Q's, but in return, finding a resonance becomes very time consuming. The top panel in Fig. 2-2(b) shows a state formed by a chain of spots with varying brightness, which collectively resonate at the same wavelength, ergo all spots including the less intense spots belong to the same coherent state that covers the entire scan interval. The "stadium-shaped" patterns are due to the cavity tip interaction [Muj07]. The bottom panel shows a different mode composed of three dominant main spots that are grouped together and show up over a dark background. It is the smallest mode that they have observed; its total spatial extent L_0 is smaller than 6 μm, which corresponds to a mode volume of ~ 2.8 $(\lambda_0/n)^3$, where n is the refractive index of the slab. Fig. 2-2(c) shows the spectral evolution of the localized mode and confirms the existence of a high confinement level both in the spatial and spectral domains. As the wavelength is tuned away from the resonance frequency λ_0, our collaborators observe that the spatial and spectral variations of the spot intensities exhibit an intricate behavior, suggesting a beating between several modes (although non-uniform coupling with the tip cannot be excluded). The inset shows the spectral evolution of the normalized intensity of the localized state and evidences a resonance with a $Q \approx$ 50,000. Since the localized mode is formed from

very tiny structural modifications, significantly smaller than those typically employed for engineered cavities, mode-profile impedance mismatch [Lal08] is kept at a very low level, and leakage into the air-clad is expected to be as small as that encountered in engineered cavities. Thus, we believe that the observed Q value is limited by the tip interaction, consistently with earlier works with silica tips and engineered cavities [Koe05].

To assert that the wavelength-scale localized mode observed is indeed due to the residual imperfections left by the fabrication facility and not to abnormally large imperfections resulting from a failure of the fabrication process, our collaborators at University of St Andrews in UK carefully analyze the W1 waveguide that produced the localized mode under a high-resolution SEM. Fig. 2-3 shows the three major defects observed in the W1 waveguide which consist in resist stains and small holes' deformations. These defects are not observed at the locations of the observed localized mode under the near-field optical microscope shown in Fig. 2-2. We can thus infer that the formation of localized modes is due to residual imperfections. This conjecture is further confirmed by the computational results that predict that wavelength-scale localized modes exist for disorder levels that are even smaller than those of the fabrication process.

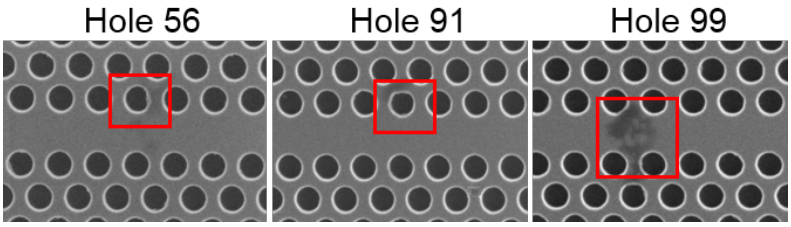

Fig. 2-3. High-resolution scanning electron microscope images of the three major defects in the W1 exhibiting localized mode. These imperfections are located at holes n°56, 91 and 99, i.e. at 23.52 µm, 38.22 µm and 41.58 µm respectively from the input facet of the W1 waveguide. Holes 56 and 91 exhibit resist stains and visible impurities around the hole. Hole 99 exhibits a resist stain and severe distortion of the hole.

2.2.2 Numerical simulations

To confirm the existence of wavelength-scale localized modes in W1 waveguides at very small disorder levels and to evaluate how frequently they are formed, we resort to statistical computations. A systematic exploration of real PhCWs with long-scale propagation lengths and nanometer perturbations is out of reach of present state-of-the-art 3D computational approaches. For this reason, we resort to a 2D fully-vectorial analysis with an effective index of 2.83 for the guided mode in the silicon slab. Out-of-plane scattering into the air-cladding is therefore omitted in the computation, but since this loss channel is much weaker than the backscattering channel near the band edge, the approximation is likely to impact only weakly our predictions on the spatial extent of the cavity modes. We consider the distribution function $P_\sigma(L_0)$, which represents the likelihood of observing a localized mode with an energy close to the band-edge cutoff-wavelength ($\lambda_c - 0.5$ nm $< \lambda < \lambda_c + 1.5$ nm) with a spatial extent smaller than L_0 at an arbitrary position along an infinitely-long W1 waveguide perturbed by a disorder level σ. $P_\sigma(L_0)$ is estimated from statistical computations (see section 2.4 for details) by averaging over 900 independent disorder realizations.

2.2.3 Spatial-extent distribution-function $P_\sigma(L_0)$

The strict protocol developed here ensures that our results are not contaminated by spurious states that may be formed by boundary artifacts due to the finite length of the computational window. $P_\sigma(L_0)$ is shown in Fig. 2-4(a) with blue curves for different disorder levels, 0.5 nm < σ < 2.5 nm.

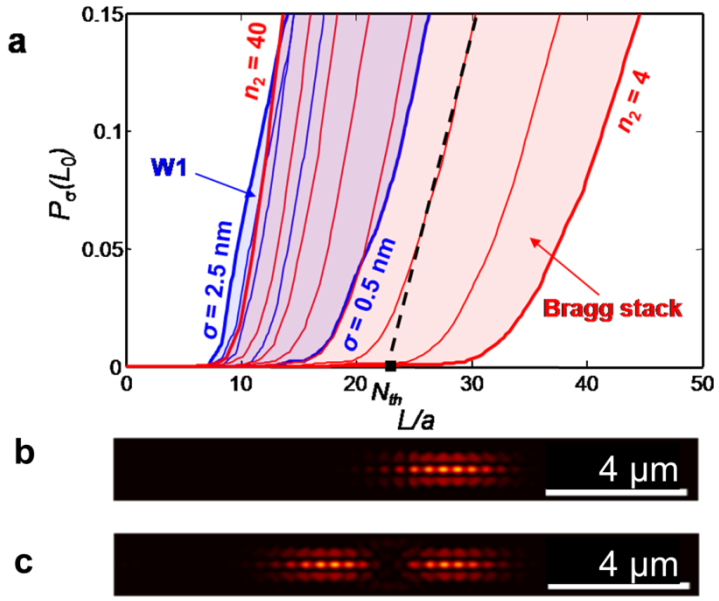

Fig. 2-4. Numerical evidence for the existence of wavelength-scale localized modes at ultra-small disorder levels. (a) Numerical prediction of the localized-mode distribution functions $P_\sigma(L_0)$ for W1 PhCWs (blue curves, from right to left σ = 0.5, 1, 1.5, 2 and 2.5 nm) and for 1D Bragg stack (red curves, from left to right n_2 = 40, 26, 19, 14, 10, 7, 5, and 4). The black dashed line represents the linear fit to obtain the threshold N_{th}. (b, c) Two striking examples of computed localized states in W1 PhCWs for σ = 1.5 nm.

The curves all exhibit a threshold-like behavior (similar to the I-V characteristic of diodes), which evidences that localized modes are formed only above a certain threshold length $N_{th}a$ (marked with a black square). The latter decreases with the disorder level and is straightforwardly estimated by a linear fit of $P_\sigma(L_0)$ for 0.03 < P_σ < 0.15. The statistical results obtained for the disorder level $\sigma \approx$ 1.5 nm of our fabrication technology support nicely the main features observed with the near-field experiments. In particular, the threshold-like behavior ($N_{th}a$ ≈ 4 μm for $\sigma \approx$ 1.5 nm) explains why cavities with spatial extents of 4 μm or less are not observed in the movie or in the high-resolution measurements. Moreover, the numerical data predicts that $P_{1.5}(L_0)$ is equal to 0.14 for the spatial extent L_0 = 6 μm of the smallest measured cavity. This implies that, on average along the W1 waveguide, localized modes with spatial extents L_0 < 6 μm are expected every $L_0/P_{1.5}(L_0)$ = 43 μm. This again supports our observation of a single localized mode when scanning a 25-μm-long section of the W1 PhCW. Finally, to further illustrate the agreement between the numerical and experimental results, in Fig. 2-4(b) we show two wavelength-scale localized modes computed for σ = 1.5 nm. The left image

corresponds to the smallest cavity (L_0 = 3.85 μm) we obtained among the 900 realizations, while the right image represents a localized state that is composed of two spots, in the spirit of the three-spotted localized mode observed experimentally and reported in the bottom panel of Fig. 2-2(b).

2.3 Theoretical model

As mentioned previously, the formation of localized modes near the photonic band-edge is completely expected, but the fact that structural imperfections as small as $\lambda/1000$ may lead to the formation of modes with spatial extents of only a few wavelengths comes more as a surprise. In engineered nanocavities for instance, the lattice structural modifications employed to create wavelength-scale gap modes are usually larger than $\lambda/1000$, typically consisting in removing, shifting or resizing a few holes [Not10; Lal08; Son05]; additionally they are spatially correlated and precisely controlled to collectively contribute to the mode formation. Thus, one would expect rather larger volumes for modes created by perturbations that are much weaker and random.

The formation of localized modes at the band-edge should rely on an intricate interplay between multiple scattering of propagating waves, which gives rise to Anderson localization, and evanescent damping due to the photonic band-gap; It should be impacted by a quantity that insures the continuity of the physics on both sides of the band-edge, which is not the case for the group velocity.

To understand the origin of wavelength-scale localized modes at tiny disorder levels, we therefore propose to establish a relation between the dispersion curves of the unperturbed waveguide, the level of geometrical variation and the spatial extent of the formed localized modes. Hereafter, we consider two geometries, the W1 waveguide previously introduced and a 1D quarter-wave thin-film stack composed of alternate layers of refractive indices n_1 = 1.5 and n_2 = 3.5, which have already been investigated quite extensively previously [Izr09; Seb06; Pod12; Kal06; Cot72]. The dispersion curves are represented in the $\omega(k_z)$ diagram of Fig. 2-5(a). In general, they are analytic and continuous at band-edges [Cot72], and can be approximated by a quadratic expression $\omega - \omega_0 = \left(\kappa - \frac{\pi}{a}\right)^2/(2m)$, where $m = (\partial^2\omega/\partial\kappa^2)^{-1}$ is the photon mass, $\kappa = k + i\alpha$ is the complex wavevector, such that $\kappa = k$ in the band and $\kappa = \frac{\pi}{a} + i\alpha$ in the gap. Fits of the dispersion curves by quadratic expressions are shown with red circles in Fig. 2-5(b).

Small geometrical variations result in energy shifts $\Delta\omega$ (see Fig. 2-5(b)) of the dispersion curve with negligible deformation [Sol04]. Thus, as it propagates in a perturbed waveguide, light alternately and randomly experiences either tunneling sections with a damping rate $\alpha = (2m\Delta\omega)^{1/2}$ or phase-shifting sections with a momentum variation $\Delta k = (2m\Delta\omega)^{1/2}$. Intuitively, in a Fabry-Perot picture, the formation of cavity modes requires both accumulating a phase-shift that satisfies a phase-matching condition (typically a 2π round-trip phase), and experiencing a strong evanescent damping (typically ≈ $1/e^2$).

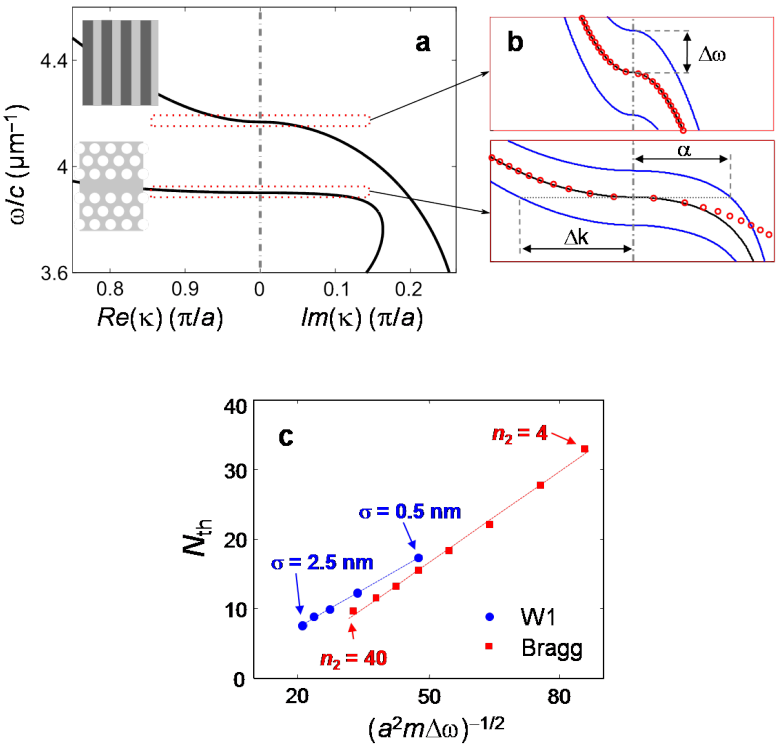

Fig. 2-5. Importance of the photon mass in the formation of wavelength-scale localized modes. (a) Dispersion curves of a 1D Bragg stack and a W1 waveguide. Note that the left and right parts of the plot correspond to the real and imaginary parts of the wavevector κ. (b) Zoomed views near the band-edge, including fits by quadratic expressions (red circles) and dispersion curves (blue lines) of the perturbed waveguides (here, $\sigma = \pm 1.5$ nm). c. Verification of Eq. (2-1) for different geometries, mass and $\Delta\omega$.

While the actual multiple-scattering process on the disordered potentials is much more involved (mainly due to varying reflection and transmission coefficients at the section interfaces), the resonance and spatial damping requirements still need to be fulfilled. This simple reasoning indicates that the minimum number of periods $N_{\min}$ required to form a cavity in a perturbed periodic system should scale as

$$N_{\min} \propto (a^2 m \Delta\omega)^{-1/2}, \qquad (2\text{-}1)$$

with a proportionality factor that primarily depends on the actual geometry, especially on the scattering coefficients at every perturbed interfaces [Maz09].

To test Eq. (2-1), we consider 1D Bragg stacks and vary the refractive index n_2 up to large (unrealistic) values, while precisely monitoring the disorder level and the period to respectively maintain $\Delta\omega/c$ = 0.01 μm^{-1} and λ_c = 1.31 μm constant. Thus the sole physical quantity that is expected to vary is the effective photon mass, from $m \times c \approx$ 0.06 μm^{-1} to 0.6 μm^{-1}. We calculate $P_\infty(L_0)$ by applying exactly the same protocol as for the W1 waveguide and by averaging over 10000 independent disorder realizations obtained by randomly varying the thicknesses of the stack layers. The P_∞'s are shown in Fig. 2-4(a) with red curves and the

corresponding threshold lengths are shown in Fig. 2-5(c) with red squares as a function of $(m\Delta\omega a^2)^{-1/2}$. Similarly, the blue dots are obtained for W1 waveguides with different disorder levels (m is constant, $\Delta\omega$ varies). As shown by the red and blue lines, N_{th} varies linearly with $(m\Delta\omega a^2)^{-1/2}$. This linear dependence obtained for different geometrical and physical parameters constitutes a firm validation of the threshold-behavior model.

Figure 2-5(c) additionally provides a direct interpretation for the surprising observation of wavelength-scale localized modes in W1 waveguides at intrinsic disorder levels, and evidences that this phenomenon cannot be observed with more classical stack geometries (except if one considers unrealistically large values for the index contrasts); it is actually the heavy mass of photons in W1 waveguides that makes the difference.

2.4 Computational method

All our computational results are obtained with an in-house fully-vectorial frequency-domain Fourier-Bloch-mode method [Sil01; Lec07a]. The strength of this method is that it relies on an analytical integration of Maxwell's equations along the PhCW axis, allowing us to study long waveguides with an S-matrix formalism which can handle Bloch modes [Lec07a]. Another unique feature of the approach is its capability to analytically satisfy the outgoing Bloch-wave conditions at the PhCW termination; this provides a high degree of accuracy to the computational results, even near the band edge cut-off. We resort to numerical integration only in the transverse x-direction with a super cell approach and Perfectly-Matched-Layers [Lec07a]. The method has already been used for many studies of periodic waveguides and has been compared to experimental investigations of real situations involving PhCW. For instance, it has been used to study various effects related to the emission of dipole sources in PhCW [Lec07b] and to the transport of light in disordered PhCWs [Bar11; Maz10].

2.4.1 Method to predict the spatial-extent likelihood of wavelength-scale localized mode

In this section, we detail the procedure that we used to determine the spatial-extent distribution-function $P_{\circ}(L_0)$ of localized modes with a spatial extent that is smaller than L_0 at any point P of a W1 waveguide (ideally infinitely long) with a disorder level σ.

The calculation of $P_{\circ}(L_0)$ raises two difficulties:

a. infinitely long waveguides cannot be handled numerically, $P_{\circ}(L_0)$ has to be predicted with waveguides of finite length L. The prediction is likely to be accurate if $L >> L_0$ and if the computed localized modes are independent of the waveguide terminations,
b. and the frequency of the localized mode is unspecified in the definition of $P_{\circ}(L_0)$ so that one needs to specify the spectral interval over which the localized mode distribution function is estimated. We choose a 2-nm-wide spectral interval $\lambda = [\lambda_c - 0.5\text{ nm};\ \lambda_c + 1.5\text{ nm}]$, because outside this interval numerical tests performed for $\sigma = 2$ nm have shown that the probability of observing a localized mode is very small.

2.4.2 Numerical layout

In order to statistically estimate $P_{\circ}(L_0)$, we consider the W1-waveguide shown in Fig. 2-6.

The waveguide is perturbed over a 100-period length and is surrounded by perfectly periodic W1-sections. The goal is to estimate $P_{\circ}(L_0)$ at a certain position. The latter is chosen to be as far as possible from the waveguide terminations to minimize boundary effects, i.e. right in the center of the waveguide, at $z = z_d = 50a$.

We first calculate the power radiated by a dipole source positioned at $z = z_d$ over the spectral interval [λ_c – 0.5 nm; λ_c + 1.5 nm], and then identify the peaks of the Lorentzian resonances of the Purcell factor (total power radiated normalized by the power radiated by the same source placed in a bulk medium). The peaks are marked by red squares in Fig. 2-7(a), Fig. 2-8(a), Fig. 2-9(a) and Fig. 2-10(a). Note that we may have several peaks at different wavelengths.

The resonances correspond to an enhancement of the local density of electromagnetic states (LDOS) and the question that arises is whether the enhancement is due to the presence of a localized mode at $z = z_d = 50a$. To get an answer, we apply a strict protocol that allows us to differentiate localized modes from other resonances.

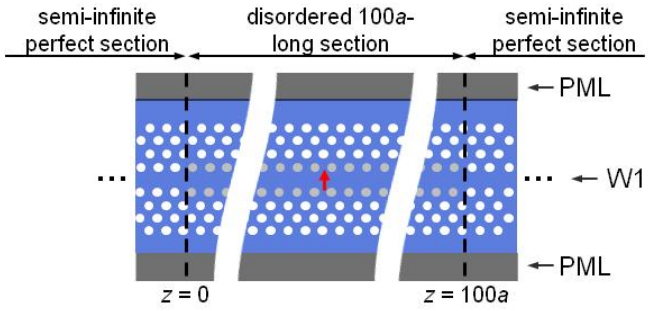

Fig. 2-6. Computational layout used for estimating $P_{\circ}(L_0)$. The red arrow represents a dipole source placed right in the center of the perturbed 100a-long section of the W1 waveguide ($z = z_d = 50a$). The grey holes of the two inner rows represent perturbed holes. Two semi-infinite W1 waveguides surround the perturbed section.

2.4.3 Protocol for determining localized modes

To determine if the resonance of the Purcell factor is due to a localized mode, a series of calculations are made:

a. We first calculate the on-axis magnetic-field profile $H_{100}(z)$ at the resonance wavelength. Four field profiles are shown as blue-dashed curves in Fig. 2-7(b), Fig. 2-8(b), Fig. 2-9(b) and Fig. 2-10(b).
b. For the same wavelength, we further calculate the field profile $H_{200}(z)$ for a 200a-long protracted waveguide. The 200a-long waveguide is obtained by surrounding the 100a-long by two 50a-long perturbed W1 sections. The disorder in the central part of the extended waveguide is strictly identical to that of the original 100a-long waveguide. The field profiles of the 200a-long W1 waveguides are shown with the red-solid curves in Fig. 2-7(b), Fig. 2-8(b), Fig. 2-9(b) and Fig. 2-10(b). Note that the 200a-long waveguide length is approximately 10 times larger than the spatial extent of the localized states whose distribution functions are being investigated.

c. In the last calculation, we shift the dipole source to the right by two periods and calculate a new field profile radiated by the shifted source for the same 200a-long W1 waveguides and for the same resonance wavelength. The Fig. 2-7(c), Fig. 2-8(c), Fig. 2-9(c) and Fig. 2-10(c) compare the field profiles radiated by the sources positioned in the center (red-solid curve) and right-shifted (dashed-dot black curves). The fields are normalized so that their maximum is one. Note that if a source excites a localized mode, the shape of the radiation field profile is expected to be independent of the source position and almost equal to the actual state profile, whereas the radiation intensity strongly depends on the position of the source.

Different cases are depicted. In Fig. 2-7, Fig. 2-8, Fig. 2-9 and Fig. 2-10 obtained for a resonance peak in the pass band of the perfect W1 waveguide, the radiation field profiles, $H_{100}(z)$ and $H_{200}(z)$, are different in shape and in intensity. The difference is stringent and evidences that the resonance of the 100a-long W1 actually depends on the waveguide termination and should not be considered as localized. For truly localized modes, the field profile should remain unchanged after extending the waveguide. In addition, we note that the mode with two lobes is likely to be a localized mode of the extended waveguide, as the ratio of the field intensity at maximum for $z \approx 47a$ is much larger than the intensities at $z \approx 0$ or 200a.

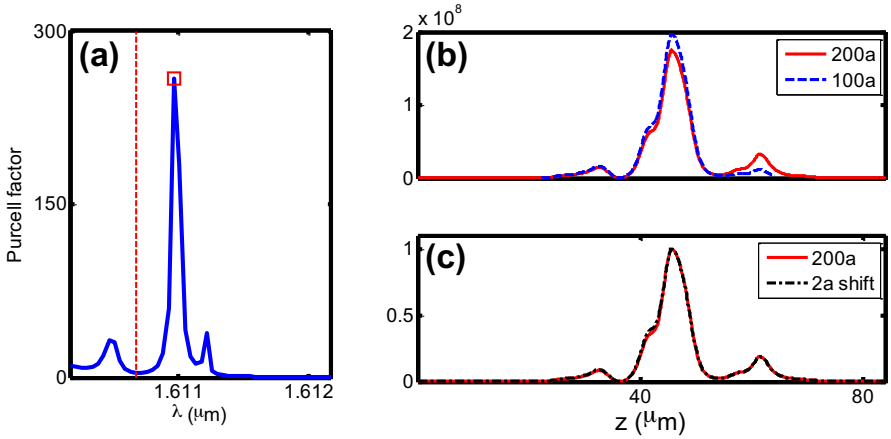

Fig. 2-7. Example of a resonance that is not accounted for in the localized mode distribution function. (a) Spectral dependence of the Purcell factor obtained for a source placed right in the center of the 100a-long W1. The vertical dashed-red line corresponds to the band-edge cutoff. (b) Magnetic-field-intensity profiles, $|H_{100}(z)|^2$and $|H_{200}(z)|^2$, at the resonance wavelength for the 100a-long W1 (dashed-blue) and the extended 200a-long W1 (red-solid). (c) Intensity profiles of the magnetic-field radiated in the 200a-long W1 for a source positioned in the center ($|H_{200}(z)|^2$ is the red curve) and for the same right shifted source (dashed-dot black). The results are obtained for $\sigma = 0.5$ nm.

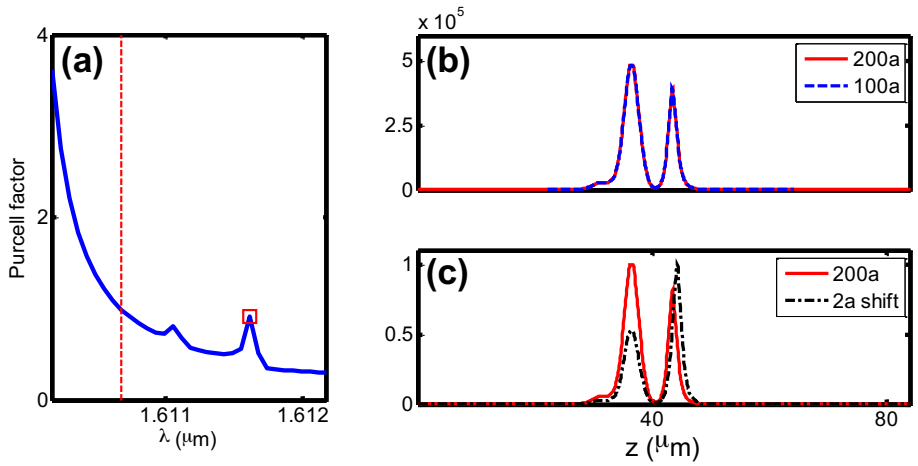

Fig. 2-8. Example of a resonance that does not qualify as a localized mode distribution function. Same as in Fig. 2-7 except that $\sigma = 0.75$ nm.

In Fig. 2-8 obtained for a wavelength in the gap, the fields radiated by the source in the original and extended W1 waveguides are virtually identical (Fig. 2-8(b)), but the profiles radiated in the extended waveguide strongly depend on the source position (Fig. 2-8(c)). Related examples are often encountered in our simulations. In general, the radiated intensity profile presents a local maximum that is located on the source position and the Purcell peak value is much weaker than the ones observed for truly localized modes.

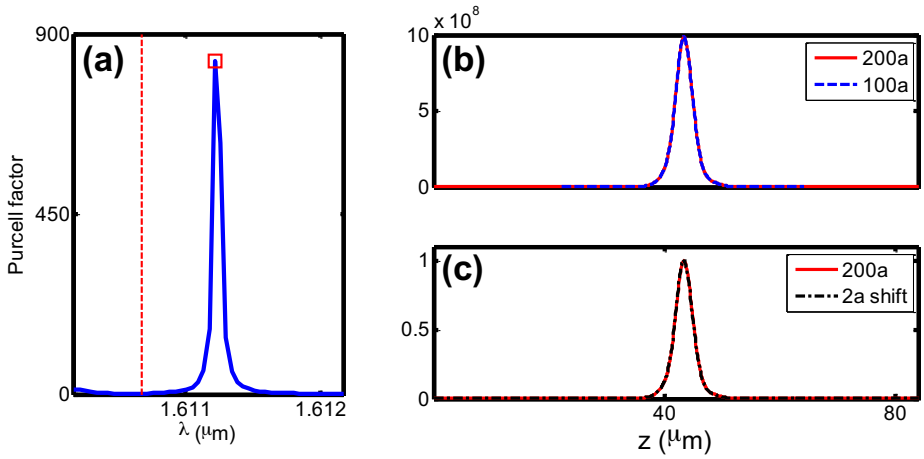

Fig. 2-9. Example of a resonance that qualifies as a localized mode by our protocol. The extension length is $L_0 = 6.4$ μm and $\sigma = 0.5$ nm.

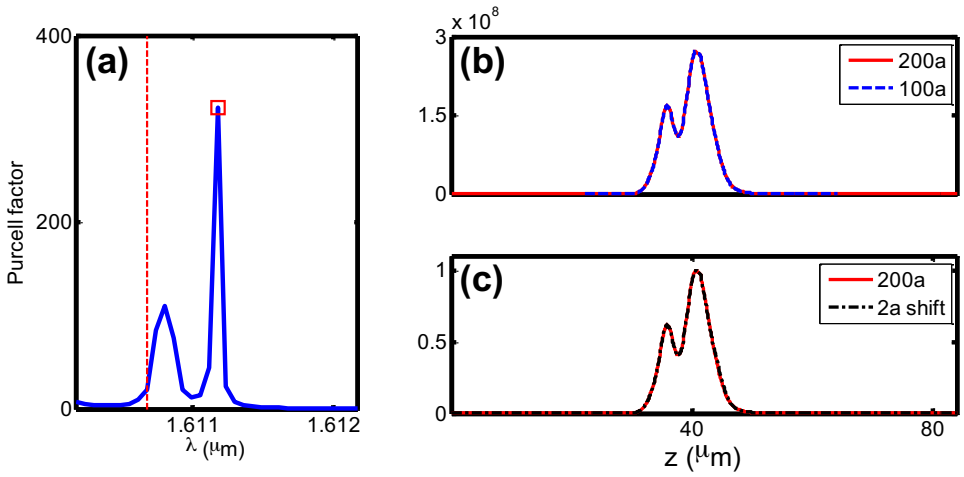

Fig. 2-10. Example of a resonance qualifies as a localized mode by our protocol. The extension length is L_0 = 12.4 μm and σ = 0.75 nm.

Fig. 2-9 and Fig. 2-10 show two resonances that qualify as localized modes using our protocol. In such cases, the Purcell factors are large (> 100), the maximum field intensity radiated by the dipole is more than four orders of magnitude larger than the intensities at the terminations of the perturbed section and the shape of the radiation field is independent of the dipole location.

In summary our protocol states that if:

a. the Purcell factor of a dipole source placed at the center ($z = z_d$) of a 100a-long randomly-perturbed W1 waveguide presents a strong peak for a resonant wavelength in the spectral interval [λ_c – 0.5 nm; λ_c + 1.5 nm],
b. the field distribution radiated by the source at resonance is the same as that calculated for an extended waveguide (suggesting that the radiated field does not depend on the waveguide termination), and
c. the field distributions radiated by two sources that are laterally shifted are proportional (suggesting that the shape of the radiated pattern does not depend on the excitation source),

then a localized mode is said to exist at $z = z_d$, provided that in addition, z_d verifies

$$z_1 < z_d < z_2, \tag{2-2}$$

where z_1 and z_2 are the localized mode boundaries defined such that the field intensity $|H_{200}(z)|$ is smaller than $max(|H_{200}(z)|/e)$ everywhere outside the interval [z_2; z_1]. Finally we then define the localized mode length L_0 as

$$L_0 = |z_1 - z_2|. \tag{2-3}$$

Although the calculations are performed for waveguides with finite lengths, we believe that the protocol is likely to represent a good estimation of the localized mode distribution function in infinite waveguides, especially when the length L_0 is much smaller than the finite lengths

(100-200a) considered in the calculations. In fact, based on the trivial statement that all modes that are localized in a finite length waveguides are also localized in an infinite waveguide, we believe that the protocol that identifies localized modes in 200a-long PhCWs underestimates the actual distribution function of infinite waveguides.

The localized-state distribution functions for PhCWs are calculated from 900 independent realizations of 100a–long waveguides for every disorder level. The same protocol is applied to the thin-film calculation, except that because of much weaker computational loads, 10,000 independent disorder realizations are used for the statistics.

2.5 Conclusion and perspective

To summarize, we have provided new understanding into the physical mechanism underlying the formation of localized modes at band-edges of periodic media, showing that the relation between the disorder level and the spatial extent of individual localized modes is driven to a large part by the effective photon mass. In particular we have investigated the possibility to form wavelength-scale localized modes at vanishingly-small disorder levels, revealing that such modes naturally form up in PhCWs at intrinsic disorder levels due to the flatness of the dispersion curve. A scaling law that relates the disorder level to the modes spatial extent is proposed and is found to agree well with the numerical and experimental results. Near-field measurements on photonic crystal waveguides and statistical numerical calculations on various structures reveal that periodic media exhibiting flat dispersion bands can support surprisingly small localized modes at almost imperceptible disorder levels ($\sigma < \lambda/1000$).

The modes have positions and frequencies that are not known in advance by design. As such, they are not easy to handle in applications that require extreme precisions, but their existence may be useful for sensing applications [Scu13], quantum electrodynamics experiments [Sap10; Gao13; Caz13] or random photonics applications [Red13; Vyn12]. The importance of the mass for light localization near photonic band-edges has not been clearly pointed out in the pioneering proposal by John [Joh87] and in follow-up research on optical localization in the slow light regime [Joh87; Top07; Moo08; Sap10; Thy12; Hui12; Izr09; Seb06; Pod12; Kal06; Not01; Vla99; Hug05a]. In the same way, it is rarely acknowledged in the literature on engineered nanocavities, such as the heterostructure family [Not10; Son05], which are defect-modes that benefit from a slow-light effect [Lal08] close to the band-edge and are in many respects similar to the present localized modes. We expect that the conceptual understanding gained from this disorder-driven study will have repercussions on future designs using defect Bloch-modes that are even heavier than the W1 waveguide mode [Mor05; Pet04] for instance, to push back the ultimate limit imposed by unavoidable disorder in engineered cavities [Tag11].

3 Theoretical treatment of atom-field interaction in periodic waveguides

In this chapter, we theoretically investigated light transport in periodic photonic crystal waveguides coupled to a two-level atom. In section 3.1, we introduce the emerged hybrid quantum systems that bear strong light matter interaction. The hybrid quantum systems combine the excellent quantum coherent properties of the ultracold atoms and high tunability of the structural dispersion curve of the nanophotonic structures. In section 3.2, by using optical Bloch equations and a photonic modal formalism, we derive semi-analytical expressions for the scattering matrix of one atom trapped in a periodic waveguide. Several important light transport properties are implicated from the scattering matrix and we illustrate the coherent light transport in a periodic nanowire formed by a chain of Si_3N_4 boxes in air. Numerically, the rigorous calculation of the scattering matrix in full space is rather challenging because the evaluation of the coupling of the quantum emitter to all the radiation modes other than the guided Bloch mode suffers numerical instability. The approximation treatment in section 3.3 allows us analytically predict the spectral response for any driving frequency and atom location. In section 3.4, we conclude that the analytical closed-form expression for analyzing the scattering of guided photons by cold atoms trapped near periodic waveguides is comfortable in practice, since it favors an in-depth understanding and allows a very efficient computation of the optical responses when some physical parameters are modified, such as the group velocity or the atom position.

3.1 Introduction

Nanophotonic structures are routinely used to enhance light matter interactions by modifying the density of virtual photon states. When an increase in the local density of states is spatially and spectrally aligned with the quantum resonance, an enhancement in the light coupling to the quantum emitter thus strong interaction between the trapped cold atoms and the launched photon modes are readily accessible. Recently, new hybrid quantum systems, combining ultracold atoms and nanostructured devices, are emerged in order to attain new paradigms in quantum measurement and processing. The combination of excellent quantum coherence properties with a very flexible platform for implementing strong interactions at subwavelength scales is expected to go beyond classical settings of all-solid-state QED with quantum dots [Lod15]. Examples include ultra-thin unclad optical fibers [Kie04; Kie05; War07], photonic-crystal cavities formed from planar dielectrics [Tho13], and more recently photonic periodic waveguides, for which the strong field enhancement at the band edge bears a high potential for atom-photon interaction [Gob14; Gob15].

3.2 Scattering matrix of single trapped atom

The core physics behind all-optical quantum manipulation with periodic waveguides is the scattering of single photons by single atoms trapped near the waveguide, which is characterized by the scattering matrix of one atom [She05]. Collective effects mediated by guided light in hybrid waveguides arise from multiple scattering between distant atoms through guided photons.

Potentially any geometry can be analysed provided that one knows propagating operators between atom pairs, scattering operators of individual atoms, and termination operators that describes how light is scattered at the waveguide facets. Indeed, modal formalisms that describe all the operators in the natural electromagnetic eigenstates (Bloch modes) of the waveguide are ideally suited to analyse collective phenomena in macroscopic hybrid waveguides that represent a real challenge for numerical method that rely on a full discretisation of Maxwell's differential equations. Bloch mode formalisms for propagation and termination operators have already been successfully developed in the context of light localization in photonic crystal waveguides [Lec07b; Sau05a; Bar11]. Here we expand this work, present a theoretical derivation of the scattering matrix of one atom [She05], and propose semi-analytical expressions that can be easily calculated. The derivation accurately considers the phase of transmitted and reflected photons, the saturation of the atom for multiphoton incident states and radiation due to imperfect atom-waveguide coupling.

We maintain the discussion at a general level, potentially with waveguides composed of lossy and dispersive materials, the dielectric geometry being a specific case. The sole assumption is that the waveguide is made of reciprocal material. The scattering-matrix derivation can be performed with a semi-classical formalism, but we rely here on a fully-quantum treatment including a quantization of the atom and photon field. The approach is based on a combination of electromagnetic Bloch-mode-expansion techniques [Lec07a] with the optical Bloch equations for the atom density-matrix operator [Gry10]. The former provides an accurate electromagnetic description of the system, including the local electric field and local density of electromagnetic states, and the latter allows us to describe the population evolution of the quantum system, assumed to be a two-level system. Both formalisms are already documented in the literature, and we do not present them again hereafter. Rather, we focus on how they are coupled to obtain the scattering matrix expression. The derivation is inspired from earlier theoretical works on the coupling of quantum emitters with translation-invariant dielectric [She05; Koj03; Man07] or metallic [Cha07; Gon11] waveguides, and coupled-resonator guides [Zho08; Cha11].

3.2.1 Quantum treatment

Let us assume that the atom can be considered as a two-level system with ground and excited states $(|\mathrm{g}\rangle, |\mathrm{e}\rangle)$ separated by frequency ω_A and that it is initially in the ground state. The atom is driven at frequency ω_L by a coherent laser field $\mathbf{E}_\mathrm{inc} = \alpha\tilde{\mathbf{E}}^{(1)}(\mathbf{r}, \omega_\mathrm{L})$, with $\tilde{\mathbf{E}}^{(1)}$ the normalized fundamental forward-propagating Bloch mode of the waveguide ($|\alpha|^2$ represents the power flow of the driving field), as sketched in Fig. 3-1.

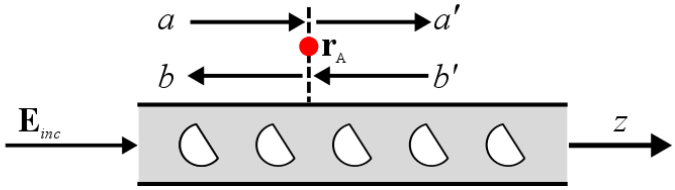

Fig. 3-1. Schematic of the hybrid system. An atom at $\mathbf{r}_\mathrm{A}$ trapped near a periodic waveguide (made from reciprocal materials) and initially in its ground state. It is driven by a guided multiphoton coherent state, launched into the

waveguide as Bloch mode $\mathbf{E}_{\mathrm{inc}}$ propagating forward at frequency ω_{L}. The scattering matrix for one atom [Eq. (3-8)] relates the scattered amplitudes, a' and b, of the Bloch mode to the incident ones, a and b'.

The interaction between the photons and the atom is described by a classical Hamiltonian

$$\widehat{H} = \int d^3\mathbf{r} \int \hat{\mathbf{f}}^{+}(\mathbf{r},\omega)\hat{\mathbf{f}}(\mathbf{r},\omega)\hbar\omega d\omega + \frac{1}{2}\hbar\omega_{\mathrm{A}}\hat{\sigma}_z - \left[\boldsymbol{\mu}\cdot\hat{\mathbf{E}}^{-}(\mathbf{r}_{\mathrm{A}})\hat{\sigma} + \hat{\sigma}^{+}\hat{\mathbf{E}}^{+}(\mathbf{r}_{\mathrm{A}})\cdot\boldsymbol{\mu}\right]. \quad (3\text{-}1)$$

The first term describes the electromagnetic field and the media, with $\hat{\mathbf{f}}(\mathbf{r},\omega)$ and $\hat{\mathbf{f}}^{+}(\mathbf{r},\omega)$ the bosonic vector field operators for the elementary excitations of the system; the second term accounts for the energy of the atom, with $\hat{\sigma}_z = |\mathrm{e}\rangle\langle\mathrm{e}| - |\mathrm{g}\rangle\langle\mathrm{g}|$ being the population difference operator; the third term accounts for the interaction between the atom and the total electric field, $\boldsymbol{\mu}$ being the transition electric dipole moment and $\hat{\sigma}$ the coherence operator. The electric field operator $\hat{\mathbf{E}}^{+}(\mathbf{r}_{\mathrm{A}})$ at the position $\mathbf{r}_{\mathrm{A}}$ of the atom consists of three contributions: the vacuum field operator, the quantized emission field of the atom, whose main ingredients are driven by the imaginary part of the classical Green tensor of the periodic waveguide and the bosonic vector field operators, and the externally driving field. By assuming that the driving field is not just a single photon, but a coherent state at frequency ω_{L} that can be treated as a classical complex field, the nonlinear response of the atom can be formally mapped to an external Rabi frequency into the optical Bloch equations, see details in [Che13] and in the method section in [Cha07]. Under the rotating wave approximation, the dynamics of the expectation values is given by optical Bloch equations and the expectation value of the total (coherent) field operator at the laser frequency can be cast into two terms [Gry10]

$$\langle\mathbf{E}(\mathbf{r})\rangle = \mathbf{E}_{\mathrm{inc}}(\mathbf{r}) + \langle\mathbf{E}_{\mathrm{at}}(\mathbf{r})\rangle, \quad (3\text{-}2)$$

where $\mathbf{E}_{\mathrm{inc}}(\mathbf{r})$ is the classical incident Bloch-mode field and $\langle\mathbf{E}_{\mathrm{at}}(\mathbf{r})\rangle$ is the expectation value of the field radiated by the atom. This general result that is valid for weak atom-field coupling regimes is not restricted to our specific waveguide geometry [Gry10]. If one further neglects the frequency shift (the Lamb shift in a vacuum electromagnetic environment) due to the self-action of the induced dipole and decoherence effects leading to time-dependent effective dipole moment, the Rabi frequency depends only on the driving laser field at the atom position and the expectation value for the induced dipole moment reads as

where $\delta = \omega_{\mathrm{L}} - \omega_{\mathrm{A}}$ is the detuning between the laser and atom frequencies, $\gamma = 2\omega_{\mathrm{L}}^2\,|\boldsymbol{\mu}|^2/(\varepsilon_0\hbar)\,\mathbf{u}^{t}\cdot Im\big(\mathbf{G}(\mathbf{r}_{\mathrm{A}},\mathbf{r}_{\mathrm{A}},\omega_{\mathrm{L}})\big)\cdot\mathbf{u}$ denotes the modified spontaneous decay rate of the excited state [Gry10], ε_0 the vacuum permittivity and $\Omega = (2\boldsymbol{\mu}/\hbar)\mathbf{u}\cdot\mathrm{E}_{\mathrm{inc}}$ is the complex external Rabi frequency. In the previous expressions, $\mathbf{u}$ denotes the polarization unit vector $\mathrm{E}_{\mathrm{inc}} = \mathrm{E}_{\mathrm{inc}}\mathbf{u}$ of the photon at the atom position and $\mathbf{G}(\mathbf{r},\mathbf{r}',\omega_{\mathrm{L}})$ is the Green tensor in the presence of the waveguide, corresponding to the electric field response at $\mathbf{r}$ to a point dipole current source at $\mathbf{r}'$. A phenomenological decay rate may be introduced in Eq. (3) to deal with dephasing decays, if necessary.

3.2.2 Electromagnetic treatment

To solve for Eqs. (3-2) and (3-3), we expand the field radiated by the atom in the complete set of optical Bloch modes, including a discrete set of truly guided modes and a continuum of radiation modes. The expectation value of the total field operator is written as

$$z > z_A, \langle \mathbf{E}(\mathbf{r}) \rangle = \sum_{p=1,N} \alpha t_p \, \tilde{\mathbf{E}}^{(p)}(\mathbf{r}) + \text{continuum}, \tag{3-4}$$

$$z < z_A, \langle \mathbf{E}(\mathbf{r}) \rangle = \alpha \tilde{\mathbf{E}}^{(1)}(\mathbf{r}) + \sum_{p=1,N} \alpha r_p \tilde{\mathbf{E}}^{(-p)}(\mathbf{r}) + \text{continuum}, \tag{3-5}$$

where z_A is the z-coordinate of the atom, r_p and t_p are the reflection and transmission amplitude coefficients, p and N denote the label and the number of truly guided modes respectively. To calculate them, one relies on a biorthogonal form that allows us to handle the orthogonality between bound and continuum states. Such forms can be mathematically derived directly from Maxwell's equations with a formalism based on the Lorentz reciprocity theorem. The formalism and its difficulties to handle leakage with continuum states is well documented in textbooks on optical waveguides [Sny84]. It was generalized to periodic waveguides in [Lec07a], by introducing complex spatial coordinate transforms that map the open problem with its associated continuum of radiation states to an approximated closed problem with a finite number of discrete states, called quasi-normal Bloch modes (QNBMs). The QNBM formalism and its biorthogonal forms have already been successfully used for several studies on periodic waveguides, for instance to calculate the coupling of quantum emitters with photonic-crystal waveguides [Lec07b], or tiny out-of-plane-scattering loss at waveguide terminations [Sau05a] or localization lengths of periodic waveguides with tiny imperfections [Bar11].

We conveniently normalize the QNBMs such that $\iint \left[\tilde{\mathbf{E}}^{(-p)}(\mathbf{r}) \times \tilde{\mathbf{H}}^{(p)}(\mathbf{r}) - \tilde{\mathbf{E}}^{(p)}(\mathbf{r}) \times \tilde{\mathbf{H}}^{(-p)}(\mathbf{r})\right] \cdot d\mathbf{S} = 4\mathcal{P}$, with S any cross-section plane of the waveguide and $\mathcal{P} = 1$. For truly-guided Bloch modes operating below the cladding light line and for non-absorbent materials, $\tilde{\mathbf{E}}^{(-p)} = -\left(\tilde{\mathbf{E}}^{(p)}\right)^*$ and $\tilde{\mathbf{H}}^{(-p)} = \left(\tilde{\mathbf{H}}^{(p)}\right)^*$, such that guided Bloch-modes have unit power flow. With this normalization, the scattering coefficients are directly obtained by considering that the atoms act as electric-dipole sources whose radiation emission feeds the waveguide QNBMs, and we have $\alpha t_p = (j\omega_L/4\mathcal{P})\langle \mathbf{d} \rangle \cdot \tilde{\mathbf{E}}^{(-p)}(\mathbf{r}_A) + \delta(p)$, with $\delta(p) = 1$ if $p = 1$ and 0 otherwise and $\alpha r_p = (j\omega_L/4\mathcal{P})\langle \mathbf{d} \rangle \cdot \tilde{\mathbf{E}}^{(p)}(\mathbf{r}_A)$. Using $\langle \mathbf{d} \rangle$ from Eq. (3-3), we obtain

$$r_p = \sigma_0 \frac{-j\varepsilon_0 c}{4\mathcal{P}} \frac{\gamma_0(2\delta_L - j\gamma)}{4\delta^2 + 2|\Omega|^2 + \gamma^2} \tilde{\mathbf{E}}^{(1)}(\mathbf{r}_A) \cdot \tilde{\mathbf{E}}^{(p)}(\mathbf{r}_A), \tag{3-7}$$

where $\sigma_0 = 6\pi c^2/\omega_A^2$ denotes the extinction cross section on resonance of an isolated two-level system and $\gamma_0 = \omega_A^3 |\boldsymbol{\mu}|^2/(3\pi\varepsilon_0 \hbar c^3)$ is the natural decay rate of the atom in a vacuum (c is the light speed). Equations (3-6)-(3-7), which constitute the main result of the present work, represent general expressions that are valid for any photonic or plasmonic waveguides and for any two-level systems. They can be extended to incorporate dephasing and

non-radiative decays [Gry10].

For atoms with prescribed quantization axes (or oriented molecules), the induced dipole is not parallel to the incident electric field; this important case can be treated as well by replacing $|\boldsymbol{\mu}|^2\mathbf{E}_{\mathrm{inc}}$ by $(\boldsymbol{\mu}\cdot\mathbf{E}_{\mathrm{inc}})\boldsymbol{\mu}$ in Eq. (3) with slightly modified expressions for γ and Ω, $\gamma = 2\omega_L^2/(\varepsilon_0\hbar)\boldsymbol{\mu}^{*t}\cdot Im\big(\mathbf{G}(\mathbf{r}_{\mathrm{A}},\mathbf{r}_{\mathrm{A}},\omega_{\mathrm{L}})\big)\cdot\mathbf{u}$ and $\Omega = (2/\hbar)\boldsymbol{\mu}\cdot\mathbf{E}_{\mathrm{inc}}$. This leads to replace $\tilde{\mathbf{E}}^{(1)}$ by $(\boldsymbol{\mu}\cdot\tilde{\mathbf{E}}^{(1)}/\boldsymbol{\mu}\cdot\boldsymbol{\mu})\boldsymbol{\mu}$ in Eqs. (5a) and (5b).

Hereafter for simplicity, we focus on the amplitude coefficients of the incident Bloch mode only. The scattering matrix for one atom, which relates the scattered mode amplitudes, a' and b, to the incident ones, a and b' (see Fig. 3-1), has the following form

$$\begin{pmatrix} a' \\ b \end{pmatrix} = \begin{bmatrix} t & r' \\ r & t' \end{bmatrix} \begin{pmatrix} a \\ b' \end{pmatrix} = \begin{bmatrix} 1+\eta\tilde{\mathbf{E}}^{(1)}\cdot\tilde{\mathbf{E}}^{(-1)} & \eta\tilde{\mathbf{E}}^{(1)}\cdot\tilde{\mathbf{E}}^{(1)} \\ \eta\tilde{\mathbf{E}}^{(-1)}\cdot\tilde{\mathbf{E}}^{(-1)} & 1+\eta\tilde{\mathbf{E}}^{(1)}\cdot\tilde{\mathbf{E}}^{(-1)} \end{bmatrix}, \tag{3-8}$$

with $\eta = \sigma_0 \frac{-j\varepsilon_0 c}{4\mathcal{P}} \frac{(2\delta_{\mathrm{L}}/\gamma_0 - j\gamma/\gamma_0)}{4(\delta/\gamma_0)^2+2(\Omega/\gamma_0)^2+(\gamma/\gamma_0)^2}$ and the Bloch mode field are taken at the atom position $\mathbf{r}_{\mathrm{A}}$.

3.2.3 Several implications from Eq. (3-8)

i) t and t' are equal (reciprocity).

ii) In sharp contrast to translation-invariant waveguides for which $\tilde{\mathbf{E}}^{(1)}\cdot\tilde{\mathbf{E}}^{(1)} = \tilde{\mathbf{E}}^{(-1)}\cdot\tilde{\mathbf{E}}^{(-1)}$ because of translation symmetry, r and r' are different in general. Thus the scattering matrices of periodic and translation-invariant waveguides are fundamentally different, and the formulas directly inspired from classical waveguide results in recent works [Gob14; Hun13] clearly overlook the phase difference between r and r'.

iii) For non-absorbent dielectric waveguides, since $\tilde{\mathbf{E}}^{(-1)} = -\big(\tilde{\mathbf{E}}^{(1)}\big)^*$, $r'/\eta = r/\eta$ and $|r'|^2$ and $|r|^2$ are equal. Perhaps counter-intuitively, this holds regardless the atom location in the unit cell of the waveguide.

iv) For metallic waveguides such as nanoparticle chains that offer deep subwavelength transverse confinements [Mai03], $|r'|^2$ and $|r|^2$ are different.

v) For small driving fields, saturation is negligible and the spectral width is given by γ. As one tunes the band edge near the atomic transition line, the total decay rate is mainly driven by the coupling to the waveguide and becomes proportional to the group index [Gob14].

For the sake of illustration, we consider a periodic nanowire formed by a chain of Si_3N_4 boxes in air, see the inset in Fig. 3-2. Despite the existence of large air gaps, remarkably low propagation losses of 2.1 dB/cm have been recently reported for this geometry at telecom wavelengths [Hal15]. Our intention is not to provide a thorough discussion of a realistic geometry with a complete design including the evaluation of Casimir–Polder forces and trapping forces with detuned lasers [Gob14; Hun13]. Rather, we intend to illustrate the meaning behind Eq. (3-8) on a simple example. All dimensions are given in the caption of Fig. 3-2. For TE–like horizontal polarization, the nanowire waveguides support a truly–guided Bloch mode and the conduction-band-edge energy coincides with the Cesium D_2 transition line at 852 nm.

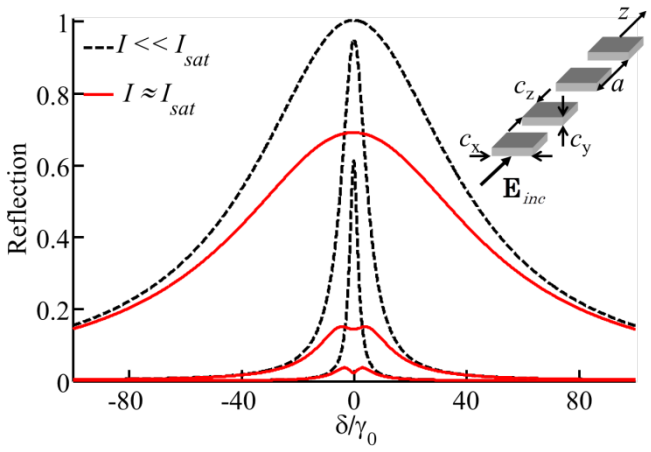

Fig. 3-2. Reflection spectra for an atom trapped in a sub-λ periodic nanowire (inset) for three values of the group index, n_g = 3,10 and 80. Black dashed curves hold for low laser intensities, and red solid curves for a laser intensity close to the saturation intensity of Cs atoms. The calculation is performed for an atom in the middle of the air gap, and for c_x = 500 nm, c_y = 100 nm, c_z = 220 nm and a = 310 nm.

Figure 3-2 shows typical reflection spectra obtained for three values of the group index n_g = 3, 10 and 80. At resonance and low excitation laser powers (black dashed curves), the photon is completely reflected for large n_g-values. As the band edge frequency is tuned near the atomic transition frequency, the atom serves as an ultranarrow filter and the incident laser field is almost completely reflected. The lineshape is the same as when a waveguide is coupled to a monomode cavity [Wak05], but more complex Fano lineshapes can be obtained for multimode waveguides as can be deduced from Eqs. (3-6)-(3-7). The red solid curves are obtained for an averaged guided power of ≈ 5 pW. For this power that corresponds to 2.1 mW/cm^2, saturation effects cannot be neglected [Ste10] and the coherent backscattering at the atomic transition frequency is reduced. At larger incident powers ($\Omega \gg \gamma_0$), most photons are directly transmitted, $|t|^2 \to 1$. Interestingly, we observe that saturation effects for the same averaged guided power are prominent at small n_g-values. This holds because the external Rabi frequency scales as $\Omega \propto n_g^{1/2}$, whereas the spontaneous emission rate of the atom scales at a much faster rate, $\gamma \propto n_g$.

3.3 Approximate treatment

The main challenge for calculating the scattering matrix is due to the emission decay into radiation modes. This requires implementing accurate outgoing wave conditions in the periodic directions. Although PML-like absorbing boundaries in periodic media have been recently optimized [Pis03], any termination breaks periodicity and numerical calculations relying on a 3D sampling is inevitably contaminated by termination backscattering, especially for small group velocities. Thus in practice, it is easier to consider finite waveguides. For instance, in a recent theoretical work [Hun13], the classical Green's tensor is not calculated for fully-periodic (infinite) waveguides, but for finite ones formed by a finite number of unit cells. Consequently the predicted spontaneous decay rate displays a series of spurious resonance peaks, from which it is difficult to infer the actual decay rate of the periodic system.

We overcame the issue by using an approach that does not rely on numerical meshing in the periodic directions, but rather on an analytical expansion in the QNBM basis [Lec07a]. The approach provides the advantage to propose virtually "exact" predictions for γ, but in turn it relies on uncommon advanced numerical tools and on calculations that need to be repeated for every atom position. Thus it is advantageous to consider an approximate treatment, in which the spontaneous decay rate in all radiation Bloch modes γ_{rad} is assumed to be equal to the emission rate in vacuum. Under this approximation,

$$\frac{\gamma}{\gamma_0} \approx 1 + \frac{3\pi c}{2\omega^2 \mathcal{P}} \left|\tilde{\mathbf{E}}^{(1)}(\mathbf{r}_{\mathrm{A}})\right|^2. \tag{3-9}$$

Together, Eqs. (3-6)-(3-7) and (3-8) allow us to analytically predict the spectral response for any driving frequency and atom location. The prediction only requires the knowledge of the driving electrical-field distribution, which is easily calculated for dielectric or metallic structures with Bloch-mode solvers.

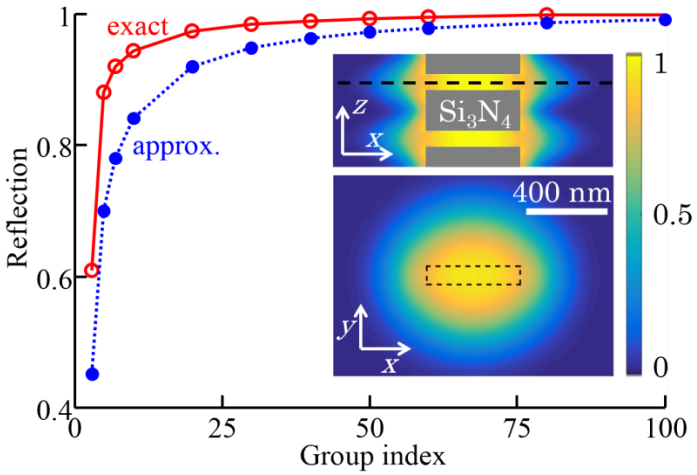

Fig. 3-3. Approximate treatment. Reflection spectra at low intensity for an atom in the middle of the air gap and matched in frequency with the driving field. The red solid and blue dotted curves are obtained with the "exact" and approximate treatments. The insets show the reflectance as a function of the atom position in the *x*-*z* and *x*-*y* (indicated by a dash line in the top inset) symmetry planes, predicted with Eq. (3-9) for n_g = 40. In the top inset, grey regions represent the Si_3N_4 boxes. On the bottom, the dash rectangle indicates the position of the Si_3N_4 box.

Figure 3-3 provides an evaluation of the error made with the approximate treatment as a function of the group index of the driving field for an atom trapped in the middle of the air gap and matched in frequency with the driving field. The approximate treatment slightly underestimates the actual back reflection. This is due to the fact that the decay into all radiation modes is smaller than the decay in vacuum ($\gamma_{\mathrm{rad}} < \gamma_0$) [Lec07b], and we have checked that the "exact" data displayed in red solid in Fig. 3-3 can be perfectly reproduced by replacing 1 by 0.4 in Eq. (3-9). The approximate treatment offers a high degree of simplicity. For illustration, we calculate the reflection at zero detuning as a function of the atom position in the *x*-*z* and *x*-*y*

planes. The results are displayed in the inset of Fig. 3-3. They are likely to be inaccurate for small reflectance but the merit is to rapidly visualize the atom positions that matter for the coupling.

3.4 Conclusion

Because they are directly expressed into the natural electromagnetic eigenstates of the waveguide, Bloch−mode scattering matrices of single atoms are an important ingredient towards the analysis of collective effects [Gob15] resulting from the strong interaction between slow photons and a collection of dilute atoms. Used at low excitation powers in conjunction with 2×2 Bloch−mode scattering−matrix−product algorithms [Bar11], Eq. (3-8) allows the study of realistic waveguides, with lengths of a few hundred period [Bar11], terminated with arbitrary facet reflectivities [Sau05a], or lossy due to absorption or to fabrication imperfections [Bar11]. The additional flexibility brought by the analytical formula, Eq. (3-9), allows fast computations that may help interpretations when some physical parameters are tuned, such as the atom positions that are not precisely known in experiments. As a final remark, let us mention that Eq. (3-8) is valid for atom−field interactions that are mediated not only by propagative photons in the band, but also for photons with energies within the gap, since the normalization does not rely on energy considerations. It implies that our theoretical treatment remains valid to study atomic interactions that are mediated by tunneling rather than propagating photons.

4 Interaction between atoms and slow light: a design study of hollow waveguide

In this chapter, we perform a design study of waveguides which offer slow light with a mode profile that is substantially pushed away in the vacuum clad, a sort of hollow core slow-light waveguide. This kind of waveguide can be of interest to implement atom-photon interactions with negligible Casimir forces. In section 4.1, we first make a quick review and address the main challenges for the emerging field of integrating on-chip nanophotonics devices and cold atoms. In section 4.2, we describe the theoretical framework for enhancing light-atom interaction intermediated by slow light and address fabrication tolerance. In section 4.3, we illustrate the design principle. In section 4.4, we show the main results that strong atom-light coupling is achieved. The last section 4.5 contains our conclusions and perspectives.

4.1 Motivation

As we have explained in chapter 3, the emerging field of integrating on-chip nanophotonics devices and cold atoms, which benefits from the advantages of both systems, can provides extremely strong light-matter interaction and may have profound impact in sensing, spectroscopy and quantum information processing. To enhance the atom-photon interaction, current approaches mainly revolve around reducing the transverse size of the light mode to the atom absorption cross section, for instance with ultra-thin unclad optical fibers [Kie05; Vet10; Kie04], and increasing the interaction time by either placing the atom in a cavity [Tho13] or reducing the light's group velocity with periodic waveguides [Gob14], which is the current topic of this work.

In the context of strong light-matter interaction implementing periodic waveguides, a long-standing obstacle is to achieve strong interaction between single atoms and single photons, while at the same time trap atoms in vacuum at large separation distances from waveguides surfaces. From fabrication prospective, another challenge that hinders the realization of strong coupling in such hybrid system is to precisely align a sufficiently slow guided mode to atomic transition line using existing semiconductor fabrication techniques. In current slow-light approaches [Gob14; Yu14; Dou15], atoms are placed inside tiny 250-nm-large slots etched into corrugated bridge waveguides and two Bloch modes operated at large detuning and at the atomic resonance are used to trap the atoms and to implement a strong photon-atom interaction. Such a combined approach represents a significant technical challenge, especially the fact that the atom is loading into the narrow interacting region [Hun13].

In this work, we outline a novel geometry that decouples the trapping and atom-field-interaction problems and offers a 2π solid-angle access to the interaction region, allowing for easy manipulations of atomic clouds around the structure. In addition, the design takes into account two important issues, which have not been considered in earlier works. Firstly, for maximizing the interaction, the atoms must be brought close to the structure in the evanescent near field. However, attractive coupling of electric dipole fluctuations (Van der Waals interactions on the subwavelength scale) sets a lower limit on the proximity of the atoms

to the nanostructure [Bar00]. It is therefore desirable to have the interacting mode extend significantly away from the surface of the structure. Secondly, because the atomic transition and the slow light frequencies should be exactly matched to precisely control the interaction strength, the waveguide fabrication requires a high accuracy, especially for weakly modulated waveguides. To weaken the requirements and to lower the impact of fabrication imperfections on slow light in general, it is therefore desirable to look for slow-light issuing from dispersion curves with large effective photon masses (i.e. flat bands). The hybrid-clad waveguide geometry proposed hereafter represents a first attempt to fulfill all those requirements.

4.2 Theoretical framework

4.2.1 Slow light for strong coupling

Let us start by considering the interaction of atoms with translation invariant waveguides, such as ultra-thin unclad optical fibers that have been being investigated as a flexible platform for implementing strong interactions between photons and cold atoms [Kie05; War07; Kie04]. For translation-invariant waveguide, the interaction is evaluated by the fraction β of the atom spontaneous decay into the guided mode of the waveguide. The β-factor can be expressed as $\beta = \gamma_{\mathrm{M}}/(\gamma_{\mathrm{M}} + \gamma')$, γ_{M} being the decay rate into the guided mode and γ' the decay rate into all other decay channels. A first route to achieve large coupling consists of enhancing the vacuum fluctuations associated with the mode of interest, so as to selectively increase γ_{M}. Alternatively, one may reduce γ'. This ambitious route that relies on the suppression of the coupling over a continuum of radiation modes has been proven successful in solid-state systems [Lec07b; Lun08] only; it is mostly unworkable for atoms in vacuum since γ' is likely to be comparable to the emission rate of the atom in vacuum γ_0, especially when the atoms are trapped far away from the waveguide. For translation-invariant waveguides, the Purcell factor is $\gamma_{\mathrm{M}}/\gamma_0 = 3/(4\pi)\, n_{\mathrm{g}}\, \lambda^2/S_{\mathrm{eff}}$ (the atom is assumed to be in air), where $S_{\mathrm{eff}} = \iint \varepsilon(\mathbf{r})|\mathbf{E}(\mathbf{r})|^2 dr^2/|\mathbf{E}(\mathbf{r}_{\mathrm{A}})|^2$ denotes the effective mode area [Sny84], $\mathbf{r}_{\mathrm{A}}$ denotes the atom position, and $\varepsilon(\mathbf{r})$ denotes the waveguide relative permittivity. It clearly indicates that the interaction is driven by two main quantities: the group index n_g and the effective photonic mode area S_{eff}. The latter was recently reduced by shrinking the optical mode using ultra-thin unclad optical fiber [2]. Consistently with [Kie05], we have calculated for the D_2 line of Cs atoms and-a 400-nm diameter fiber, that the beta factor is only 0.07 at the fiber surface ($d = \lambda/2$). In comparison, a photonic structure that would maintain the same effective mode area and additionally increase the group index to $n_{\mathrm{g}} \approx 50$ would reach $\beta \approx 0.79$. One immediately sees the promising potential of periodic photonic waveguides that operates in the slow light regime [Gob14; Hun13; Zan15]. Note that metallic waveguides such as chains of metallic nanoparticles that offer deep subwavelength transverse confinement [Mai03] may also be of high potential interest.

4.2.2 Effective mass for robustness design

Now that we have established the necessity to implement slow light for strong photon-atom coupling (strong coupling may be ambiguous), let us go one step further and consider requirements imposed by the precise matching of the atom frequency ω_{A} with the slow-light frequencies of the photonic band. With the thick dispersion curve $\omega(k)$ in Fig. 4-1, we

illustrate an ideal world for which the atomic frequency is perfectly matched with a desired group velocity v_0 achieved at $\omega = \omega_A$ for nominal parameters.

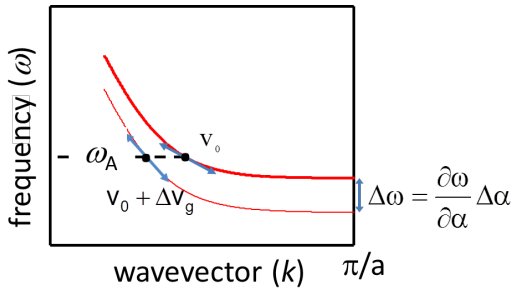

Fig. 4-1. Robustness to fabrication fluctuations near the boundary of the first Brillouin zone. The ideal dispersion curve (bold line) with the targeted group-velocity v_0 at the atom-line frequency ω_A is shifted to the actual dispersion curve (thin line) because of uncontrolled fabrication fluctuations. The actual group velocity is $v_0 + \Delta v_g$ at $\omega = \omega_A$.

In real world because of uncontrolled fabrication fluctuations, waveguides are never manufactured with their nominal parameter values. The thin curve in Fig. 4-1 represents a realistic version of the dispersion curve, which is vertically shifted by $(\frac{\partial\omega}{\partial\alpha})\Delta\alpha$ due to tiny fabrication errors $\Delta\alpha$ of the waveguide parameters. The actual group velocity is not the desired one v_0 and is shifted by $\Delta v_g = \left(\frac{\partial v_g}{\partial\omega}\right)\left(\frac{\partial\omega}{\partial\alpha}\right)\Delta\alpha$.

$$\Delta v_g = \frac{1}{m v_0}\frac{\partial\omega}{\partial\alpha}\Delta\alpha \qquad (4\text{-}10)$$

where m is the effective mass of the photon dispersion curve. Equation (4-10) also represents small group-velocity mismatches experienced by light that see inevitable fabrication imperfections $\Delta\alpha$ as it propagates in a waveguide. It has a general nature, which essentially underlines that operation at small group velocities imposes strong requirements on the quality of the fabrication processes and that the effects of fabrication fluctuations can be minimized by selecting waveguide geometries with large effective mass (i.e. flat bands). Let us note that the frequency shift $\Delta\omega = (\frac{\partial\omega}{\partial\alpha})\Delta\alpha$ is difficult to lower by design since close to the band edge, these shifts are directly proportional to variations of the waveguide effective index n_{eff}, $\frac{\Delta\omega}{\omega} = \frac{\Delta n_{\text{eff}}}{n_{\text{eff}}}$. By using a power-series expansion $\omega - \omega_A = v_0(k - k_A) + \frac{1}{2}a_0(k - k_A)^2 + \cdots$ of the dispersion curve instead of a parabolic approximation, one essentially obtains the same conclusion that robust design is achieved for small group-velocity dispersion (i.e. small a_0's).

4.3 Design

4.3.1 Photonic crystal versus Bragg waveguides

In Bragg-type periodic waveguides, guidance is achieved by total internal reflection on the waveguide lateral clad walls and light slowdown results from multiple reflections due to the

periodicity. Examples of Bragg-type waveguides are sub-λ periodic chains [Hal15], nanowires perforated by holes [Vel06] or corrugated slot waveguides [Gob14; Hun13]. Such index-guided waveguides operate much like one-dimensional Bragg stacks and it is difficult to tailor strongly their dispersion curve. Their effective mass, which is proportional to the refractive index modulation, is very small especially if light is expelled out of the waveguide into the air clad.

In contrast, for photonic crystal waveguides, guidance is mainly due to light reflection on a photonic band gap, and by tuning some geometrical parameters, the phase of the reflection coefficient can be made highly dispersive [Sau05b]. As a result, the dispersion curve and the group-velocity-dispersion can be engineered even for small group velocities [Fra06], and the effective mass can reach high values that are out of the reach of Bragg-type periodic waveguides [Fag15].

The proposed hybrid-clad waveguide (see Fig. 4-2(a)) combines the two guidance mechanisms. On one lateral side of the waveguide, the fundamental mode is gap-guided by a periodic array of holes, which allows us to control the flatness of the dispersion band, and on the opposite lateral side, the mode is index-guided by a sharp vertical sidewall, which offers an entire half space to host the electric field expelled into the vacuum cladding. This half space may be used to approach another collinear waveguide (potentially fabricated on the same wafer), which may be translation invariant and may be used to trap the atoms; by decoupling the trapping and atom-field-interaction functionalities, better flexibility is expected.

4.3.2 Hybrid-clad waveguides

The design faces two conflicting perspectives. On one side, to implement an atom-photon interaction that occurs away from the nanostructure, one needs to synthesize a Bloch mode with a field that well expels into the vacuum cladding. This implies that the Bloch mode weakly interacts with the periodic structure. On the other side, to control slow-light properties, one needs a strong interaction between the Bloch mode and the periodic modulation, keeping away from any weak-permittivity-modulation regime for which the slowness of the Bloch mode and the flatness of the band are hardly controllable. Thus the design appears as a pure exercise of compromise, with the hybrid-clad waveguide of Fig. 4-2(a) being a first initial try.

The dispersion curve of the hybrid-clad waveguide is calculated with a mode-solver initially developed for studying light propagation in photonic crystal waveguides operating above the light cone [Lal02] and further refined to study light transport in periodic waveguides [Lec07a]. The solver relies on an analytical integration of Maxwell's equations along the periodic direction and on a supercell approach with real, nonlinear coordinate transforms (stretched-coordinate PML) [Hug05b] in the two other transverse x- and y-directions. The transforms allow us to carefully handle far-field radiation conditions, even when the guided mode penetrates far away in the vacuum cladding. The supercell includes 9 rows of holes on one side and a 1-µm-large vacuum gap on the other side, for a total area of $4 \times 0.5\ \mu m^2$. The numerical sampling in the transverse directions is performed in the Fourier domain using truncated Fourier series. All numerical results are obtained by retaining a total number of 51×29 Fourier harmonics, but other calculations performed for larger truncation orders have revealed that the truncation error has no influence on the following analysis.

The first step of the design consists in finding the range of photonic crystal parameters a and

r, for which the photonic crystal membrane offers a TE–like bandgap for the Rubidium D_2 transition line at $\lambda_{Rb} \approx 780$nm. The calculations are performed with the MIT Photonic-Bands (MPB) package [Joh01]. After choosing some parameter data, in a second step, we monitor the light-channel width L to shift the band edge of the dispersion curve close to the light line. This step is pivotal to obtain a slow Bloch mode with a field distribution that penetrates away into the vacuum clad. As L is reduced, the dispersion curve shifts towards high frequencies; however as the band-edge approaches the vacuum light line, we observe that the computation of the mode becomes unstable, as if the mode couples to the continuum of radiation states at slow group velocities. We have performed several tries, repeating the second step for different values of a and r.

We assume that the waveguide is etched into a 300-nm-thick Silicon nitride (SiN)[①] membrane. Photonic crystal structures based on SiN and fabricated with electron-beam writers and dry etching have already been manufactured for visible-light applications with great accuracy [Mak06; Bar08]. The photonic crystal is formed by cylindrical holes perforated in the membrane on a triangular lattice. The propagation direction z coincides with the Γ-K direction of the crystal. The hybrid-clad waveguide depends on four parameters, the membrane thickness h, the lattice period a, the hole radius r and the channel width L.

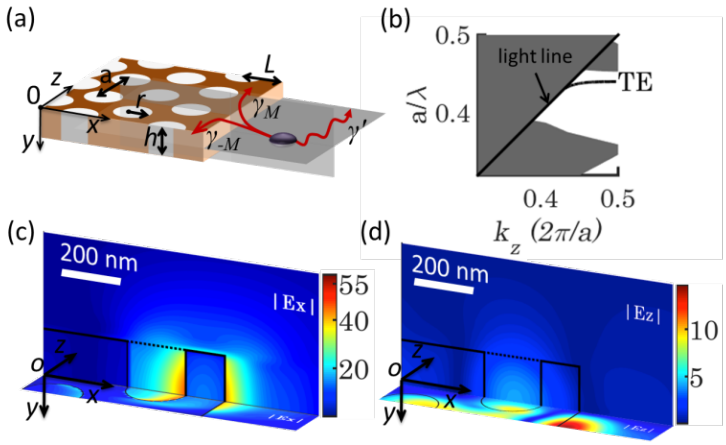

Fig. 4-2. TE-like mode of the hybrid-clad waveguide. (a) Sketch of the hybrid-clad waveguide (only four rows of air holes are shown on the left side of the waveguide). The atoms decay into the fundamental guided mode and the continuum of radiation modes with decay rates γ_M and γ_{rad}, respectively. (b) Dispersion curve of the fundamental TE-like Bloch mode. The grey region indicates the extended band of the photonic crystal membrane. The vacuum light line is shown with the red line. (c-d) Distributions of the dominant electric-field components ($|E_x|$, $|E_z|$) in two symmetry planes for $n_g = 50$.

Figure 4-2(b) shows the dispersion curve of the TE-like mode of the hybrid-clad waveguide

[①] Silicon nitride (SiN) is transparent over a broadband including the visible [Stu77] that covers our interested wavelength *780 nm*. It is also compatible for current CMOS fabrication technology [Ike08; Lev09]. Photonic crystal structures based on SiN have been studied for visible applications [Net00; Mak06; Bar07].

for a = 340 nm, r = 0.3a, h = 300 nm, and L = 240 nm. For this set of parameters, the hybrid-clad waveguide is monomode in the band gap. Figure 4-2(c) displays the distributions of the dominant electric-field components in the symmetry planes of the hybrid-clad waveguide (note that the *y*-component of the electric field is null in the *x*-*z* plane for TE-like modes). The calculation is performed for a group index of 50, but very similar results are obtained for other group indices, n_g = 10-100. The electric-field distribution is primarily intense in vacuum, in the first and second rows of holes and more importantly in the vacuum cladding on the right side of the vertical sidewall. This observation holds for all field components, irrespective of their continuous or discontinuous character at the hole or sidewall interfaces. Additionally if we pay attention to the light-blue areas rather than to the red intense spots, we note that the mode expels quite far away above the membrane and on the right side of the vertical sidewall, indicating that strong atom-photon couplings at large transverse separation-distances is possible.

4.4 Atom-field coupling

An important figure of merit [Gob14; Zan15] that characterizes the strength of the atom-photon coupling is the single-atom reflectivity. The latter can be defined as the reflection of a coherent multiphoton laser field at frequency ω_L launched into the fundamental Bloch mode of the waveguide and illuminating a single atom initially in its ground state. During the interaction, the incident photons first polarize the atom with an induced dipole moment that is proportional to the driving Bloch-mode field-vector $\mathbf{E}(\mathbf{r}_A, \omega_L)$ at the atom position $\mathbf{r}_A$, and then the atom radiates by exciting the guided mode and all other radiation modes with decay rates γ_M and γ'.

This scattering problem has been recently analyzed with a fully-quantum treatment based on a combination of electromagnetic Bloch-mode-expansion and Green-tensor techniques with the optical Bloch equations for the atom density-matrix operator. In the weak coupling regime and for a two-level atom, it was shown that the Bloch-mode reflection coefficient is given by [Zan15]

$$r = \sigma_0 \frac{-j\varepsilon_0 c}{4} \frac{(2\delta/\gamma_0 - j\gamma/\gamma_0)}{4(\delta/\gamma_0)^2 + 2|\Omega/\gamma_0|^2 + (\gamma/\gamma_0)^2} |\mathbf{E}(\mathbf{r}_A, \omega_L)|^2 \qquad (4\text{-}11)$$

where $\delta = \omega_L - \omega_A$ is the detuning between the laser driving frequency and the atom resonance frequency ω_A, $\sigma_0 = 6\pi c^2/\omega_A^2$ denotes the extinction cross section on resonance of an isolated quantum mechanical two-level system, ε_0 the permittivity of vacuum, c the light speed, Ω is the complex external Rabi frequency which takes into account eventual saturation effects and $\gamma = \gamma_M + \gamma'$ is the total decay rate in all the photon modes. Equation (4-11) holds for an electric field that is normalized such that the Bloch-mode power flow is unitary. The challenging part for calculating γ is the calculation of the total decay that necessitate to evaluate the coupling into radiation modes. However by assuming that $\gamma_{rad} = \gamma_0$, the total decay rate takes a simple expression $\gamma/\gamma_0 \approx 1 + (3\pi c/2\omega^2)|\mathbf{E}(\mathbf{r}_A, \omega_L)|^2$, and the reflection coefficient, which is slightly underestimated, is straightforwardly calculated for any driving laser frequency and for any atom location [Zan15].

In Fig. 4-3, we display the reflectance distribution at zero detuning as a function of the atom position in the main symmetry planes. Several values of the group velocity are considered,

$n_g = 2$, 10, 50 and 100 and saturation effects are neglected. Figure 4-3(a) is related to the *x*-*z* horizontal median plane (see Fig. 4-2(a)), in which only the *x*- and *z*-components of the electric field are involved in the atom-waveguide coupling, and Fig. 4-3(b) to the *x*-*y* vertical plane (see Fig. 4-2(a)), in which all field components are involved. Owing to the diminishing group velocity, large reflectance values are obtained when the atomic line frequency is matched with the photonic resonance. Importantly, we note that strong atom-photon couplings are predicted for large separation distances Δx from the vertical sidewall. For example, the resonant reflectance for a moderate n_g value of 50 is $|r|^2 = 0.9$ for atoms that are trapped in the horizontal median plane at $\Delta x = 200$ nm from the sidewall. Such a strong atom-photon coupling at large separation-distances, for which Van der Waals interactions induced by random electric dipole fluctuations are negligible especially with silicon nitride structures, is unprecedented in atomic/molecular optical physics and could create new opportunities for high precision studies.

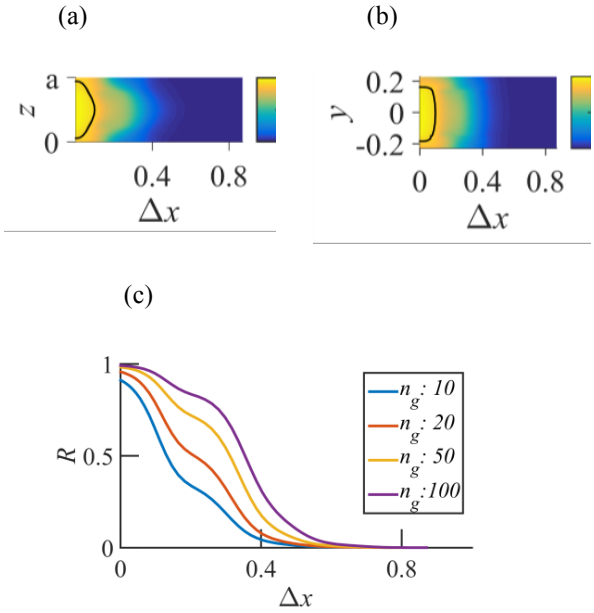

Fig. 4-3. Reflectance of a single atom for $\omega_L = \omega_A$ as a function of the atom position in the symmetry planes for $n_g = 50$. (a) *x*-*z* horizontal plane in Fig. 4-2(a). (b) *x*-*y* vertical plane in Fig. 4-2(a). (c) Reflection in the line ($y = 0$, $z = a/2$). The black contour line indicates a reflectance of 0.9 and $\Delta x = 0$ corresponds to the sidewall boundary.

4.5 Conclusions

Indeed there are challenges in the implementation of hybrid systems composed of cold atoms trapped in the near field of optical nanostructures, including atom loading, light scattering from device imperfections, atom-photon resonance matching, robustness to vacuum-force fluctuations. In general, slow light is a consequence of mode fields interacting with a periodic structure. Efficient light slowdown can be achieved when the mode field propagates inside a corrugated channel medium; however, this fact conflicts with the desire for implementing flat dispersion bands with a mode field that dominantly resides in the vacuum cladding where the atoms are loaded.

The present design that uses slow-light in photonic crystal waveguides is certainly not optimal, but it offers the benefit to directly address the conflict and to present a compromised solution. We are working toward extensions of this work with more complicated geometries by numerical simulation and device fabrication. Our efforts are motivated by the predictions in Fig. 4-3, which may lead to a new generation of devices offering a strong photon interaction with atoms that are trapped with negligible vacuum-force interaction.

Fabrication imperfections of current technologies do not allow the exact prediction of spectral position of the mode. As the waveguide is operated in the slow light regime where v_g is small, the group velocity mismatch is all the more stringent since the group velocity varies rapidly with the frequency shift. It explains why significant slow light is not observed in such hybrid system recently (nanostructures with small mass and large group velocity mismatch [Gob14]).

5 Numerical Issues

In this chapter, we numerical issues related to the simulations performed in chapters 3 and 4 (simulations made in chapter 2 were in 2D and the convergence is excellent). Firstly, we describe the numerical method, i.e. the aperiodic Fourier modal method (a-FMM) in section 5.1. As a generalization of FMM, the a-FMM can deal with non-periodic structure by artificial periodization via the implementation of Perfectly Matched Layer. An appropriate formulation of Maxwell's equations and adaptive spatial resolution method is used to increase the calculation efficiency. To evaluate the scattering properties of a single atom in chapters 3 and 4, it is convenient as explained in section 5.2.1 to normalize the modal profile with a numerical trick that we call the "double pesée". In section 5.2.2, we then present the "double pesée", which is a useful technique in the numerical analysis of photonic crystal waveguides, especially when light expend far away in the cladding. We show in section 5.2.3 that the study of the emission by a magnetic dipole source in the waveguide allows us to provide an accurate normalization of the mode. In section 5.2.4 and 5.2.5, we study the numerical accuracy and present the convergence performance of the coefficients of the scattering matrix of a single atom. In addition, we also analyze how the accuracy is affected by the mode confinement. The last section 5.4 concludes and summarizes and discusses further possible improvement.

5.1 Numerical method

Throughout the thesis, the numerical simulations have been performed with our in-house software which is a concrete implementation of Fourier modal method (FMM). This method is also called rigorous coupled-wave analysis (RCWA) and has been gradually developed for the rigorous analysis of the electromagnetic waves diffraction by gratings [Moh81; Moh95]. As the name Fourier modal method suggests, all the electromagnetic field components and the material functions are expanded into Fourier series in terms of spatial harmonics. However, the spatial discretization and finite truncation of Fourier series that are required by the concrete numerical implementation result in the deviation of the numerical results from the exact values. For a long time, the numerical performances of Fourier expansion techniques have been plagued by slow convergence performances, which have been believed to be caused by Gibbs-related phenomena resulting from the use of Fourier series to expand discontinuous functions [Li93; Vil94]. A dramatic improvement in the convergence rate has been achieved for TM polarization of one-dimensional gratings [Gra96; Lal96]，as well as for the general case of conical diffraction [Lal96]. This finding was followed by the derivation of mathematical theorems that govern the factorization of Fourier series, i.e. Fourier factorization rules [Li96b]. It implies that an appropriate formulation of the eigenvalue problem and the correct Fourier factorization must be carefully performed to assure fast convergence rate. These works had a tremendous impact on the performances of theories relying on Fourier expansion techniques for solving Maxwell's equations in periodic media and earlier methods have been rapidly revisited and improved. Examples of improvements are the Fourier modal method for crossed gratings [Li97], the differential method [Pop00] and the plane-wave method for band computations of photonic crystals [Lal98], to quote only a few of them.

5.1.1 a-FMM: implementation of Perfectly Matched Layer

The a-FMM (where "a" denotes "artificially periodic, or aperiodic for short") is a generalisation of the FMM approach that allows the method to handle non-periodic situations, e.g. photonic crystal waveguides, by artificial periodization via the introduction of a Perfectly Matched Layer (PML) [Lal00; Sil01] or of complex nonlinear coordinate transformations [Hug05b]. The PMLs relying on a complex nonlinear coordinate transform which maps the two semi-infinite half spaces surrounding the investigated device geometry into a finite space. Theoretically, this mapping guarantees that the outgoing wave conditions are perfectly satisfied since evanescent or propagative fields, *incoming* from the boundaries of the computational domain, are attenuated over an infinite distance between reaching the device. The mapping [Hug05b], which is implemented as a modification of the differential operators, appears as a generalization of more classical PML-formulations [Che94; Sac95], which are seen as a renormalization of the permittivity and permeability distributions.

For photonic crystal waveguides, the artificial periodization along the transverse directions makes the field periodic, which allows to expand the electric field $\boldsymbol{E}$ and magnetic field $\boldsymbol{H}$ into a Fourier basis [Sil01],

$$\mathbf{H}(\mathbf{r}) = \sum_{p,q} (U_{xpq}\,\mathbf{x} + U_{ypq}\,\mathbf{y} + U_{zpq}\,\mathbf{z}) \exp(jpG_x x + jqG_y y), \tag{5-1}$$

$$\mathbf{E}(\mathbf{r}) = \sum_{p,q} (S_{xpq}\,\mathbf{x} + S_{ypq}\,\mathbf{y} + S_{zpq}\,\mathbf{z}) \exp(jpG_x x + jqG_y y), \tag{5-2}$$

where $G_x=2\pi/\Lambda_x$ and $G_y=2\pi/\Lambda_y$, Λ_x and Λ_y being the lengths of the unit cell of the transverse section. In Eqs. (5-1) and (5-2), the $S_{\alpha lm}$ and $U_{\alpha lm}$ (α=x, y or z) are unknown z-dependent coefficients. In practice, the Fourier series have to be truncated, so we denote by m_x and m_y the truncation ranks, $-m_x<p<m_x$ and $-m_y<q<m_y$. By incorporating expressions (5-1) and (5-2) into the curl Maxwell's equations, and by expanding the permittivity and the permeability in the Fourier basis as well, we obtain after elimination of the z-components [Lal02]

$$\frac{1}{k_0}\frac{d[\boldsymbol{\Psi}]}{dz} = \boldsymbol{\Omega}(z)\,[\boldsymbol{\Psi}], \tag{5-3}$$

In Eq. (5-3), $\boldsymbol{\Psi}$ is equal to $[\mathbf{S}_x\ \mathbf{S}_y\ \mathbf{U}_x\ \mathbf{U}_y]$, a column-vector formed by the electric- and magnetic-field coefficients and $\boldsymbol{\Omega}$ is a matrix formed by the Fourier coefficients of the permittivity and of the permeability. The matrix $\boldsymbol{\Omega}$ in Eq. (5-3) depends on the variable z since the permittivity function is z-dependent.

5.1.2 Scattering Matrix

The calculation of QNBMs requires the integration of Eq. (5-3) over a unit cell from z to $z + a$. For the integration, we approximate the real profile of the circular holes by a stack of slices with locally z-invariant permittivities [Lal02]. We have used $N_s = 9$ slices per holes, i.e. a z-discretisation step of $\approx \lambda/35$. Indeed, the accuracy of the computational results increases as N_s

increases, but calculations performed for N_s=19 have revealed that the discretisation error is much smaller than the truncation errors discussed hereafter. Within this approximation, the integration along the z-direction can be performed analytically. The N local modes of each slice (p) can be called quasi-normal modes (QNMs) as they correspond to the mode of a z-invariant waveguide surrounded by PMLs [Sil01]. The QNMs, denoted by the vectors $\mathbf{W}_n^{(p)}$ and $\mathbf{W}_{-n}^{(p)}$ (n=1,…N) in the Fourier basis, are calculated in every slice (p) as the eigenvector of a local matrix $\mathbf{\Omega}^{(p)}$. Denoting by $\lambda^{(p)}$ the corresponding eigenvalue (the QNM propagation constant), the electromagnetic fields $\mathbf{\Psi}^{(p)}$ can be written as a superposition of QNMs in very slice (p)

$$\mathbf{\Psi}^{(p)} = \sum_{n=1}^{N} b_n^{(p)} \exp(-\lambda_n^{(p)} z)\, \mathbf{W}_n^{(p)} + f_n^{(p)} \exp(\lambda_n^{(p)} z)\, \mathbf{W}_{-n}^{(p)}, \tag{5-4}$$

where $\mathbf{b}^{(p)}$ and $\mathbf{f}^{(p)}$ are column vectors whose elements are the amplitudes of the QNMs propagating backward (in the negative z-direction) and forward (in the positive z-direction), respectively. The linearity of Maxwell's equations assures the existence of a linear relationship between the mode amplitudes of the slice (i), $\mathbf{b}^{(i)}$ and $\mathbf{f}^{(i)}$, in the input z-plane and those of the slice (t), $\mathbf{b}^{(t)}$ and $\mathbf{f}^{(t)}$, in the output (z+a)-plane. To avoid any numerical problems, an S-matrix approach is used to relate these amplitudes. In a compact form, we have

$$\begin{bmatrix} \mathbf{b}^{(i)} \\ \mathbf{f}^{(t)} \end{bmatrix} = \begin{bmatrix} \mathbf{S}_{11} & \mathbf{S}_{12} \\ \mathbf{S}_{21} & \mathbf{S}_{22} \end{bmatrix} \begin{bmatrix} \mathbf{b}^{(t)} \\ \mathbf{f}^{(i)} \end{bmatrix}, \tag{5-5}$$

where the matrix on the right-hand side of the equation is simply the S-matrix of a unit cell. Details concerning the recursive calculation of S can be found in [Li96a].

In brief, the method relies on an analytical integration of Maxwell's equations along the incident direction and on a supercell approach in the two others transverse x- and y-directions [Hug05b]. Periodic boundary conditions are used in the incident direction and PMLs implemented as nonlinear complex coordinate transforms are additionally incorporated on the boundaries of the supercell in order to handle out-of-plane far-field radiation in the air clad. Since these PMLs absorb non-evanescent radiations, the electromagnetic fields are null on the transverse boundaries of the supercell and are thus periodic functions of the transverse coordinates. This allows the calculation of the radiated and guided modes in a Fourier basis in each layer (the hemi-ellipsoidal bumps are discretized in a series of thin uniform layers in the incident direction) and the integration in the incident direction by relating recursively the modes amplitudes (Eq. 5-4) in the different layers using a scattering matrix approach (Eq. 5-5).

5.1.3 Adaptive spatial resolution

We have mentioned in the beginning of section 5.1 that the correct Fourier factorization of products of discontinuous periodic functions in FMM may greatly improve the convergence performance. However, the FMM still presents intrinsic weakness, e.g. the FMM converges slowly in case the permittivity functions exhibit simultaneously high contrast and narrow geometrical details even if the correct Fourier factorization of products of discontinuous periodic functions is applied. This difficulty arises from the fact that the spatial resolution in the

usual FMM remains uniform, irrespective of the material profile. It can be overcome by increasing spatial resolution (dilatation) around the discontinuities through real coordinate transform, as demonstrated by the red solid lines in Fig. 5-1 [Bes07]. On the other hand, we can also have spatial compression (blue dotted lines in Fig. 5-1) when the material function is slowly varying or constant over large computational domains to save computational time. It is worth mentioning that PML can be viewed as a complex coordinate transform as indicated by the black dashed lines in Fig. 5-1.

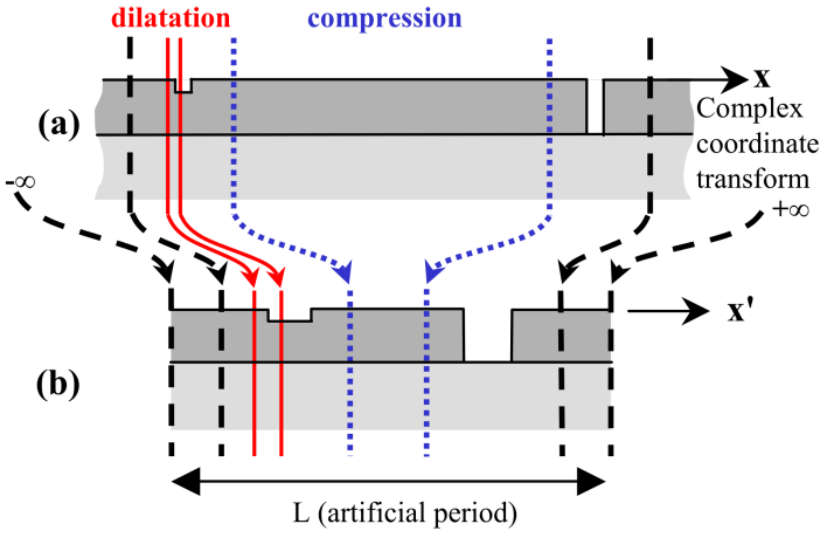

Fig. 5-1. Real and complex coordinate transforms. The coordinate transforms map the real space (a) to the computational space (b). Black dashed lines: nonlinear complex coordinate transform (PML) to satisfy outgoing wave conditions for $x \to \pm\infty$. Dotted blue lines: real PML-like compression transform used for reducing the transversal size L of the computational window. Solid red lines: real dilatation PML-like transform used for enlarging in the new space the vertical silver-air boundaries. This transform is applied four times, but for the sake of clarity, only the left boundary transform is shown. Note that the transversal dimension *x'* in the computation space is regularly sampled in the Fourier domain.

5.2 Convergence performance and accuracy

In chapters 3 and 4, we theoretically studied the interaction between cold atoms and guided Bloch modes in photonic crystal waveguides, when the atom frequency is matched with the slow-light region of the waveguide close the band edge.

5.2.1 Calculation of the guided Bloch mode in hybrid-clad waveguide

The accurate calculation of the fundamental TE-like guided Bloch mode is important. The Bloch mode is calculated by solving the source-free Maxwell's equations

$$\nabla \times \mathbf{E} = \mathrm{j}\omega\boldsymbol{\mu}(\mathbf{r})\mathbf{H}, \tag{5-6}$$

$$\nabla \times \mathbf{H} = -\mathrm{j}\omega\boldsymbol{\varepsilon}(\mathbf{r})\mathbf{E}, \tag{5-7}$$

where ω is the frequency, $\boldsymbol{\varepsilon}(\mathbf{r})$ and $\boldsymbol{\mu}(\mathbf{r})$ are the permittivity and permeability of the waveguide. The Bloch modes are denoted by $\boldsymbol{\Phi}^{(m)} = \left[\mathbf{E}^{(m)}, \mathbf{H}^{(m)}\right] e^{jk_m z}$, where k_m is the wave vector of the Bloch mode, $\mathbf{E}^{(m)}$ and $\mathbf{H}^{(m)}$ are the modal electric and magnetic field components.

To analyze the convergence of one concrete numerical problem, it is better to compare the numerical value the exact value. But most problems do not have analytical solutions, like the Bloch modes in the hybrid-clad waveguide and sub-wavelength periodic nanowire considered in chapters 3 and 4. For this reason, to evaluate the accuracy of the modes computation, we purely rely on numerical tests.

First, we calculate the effective index of the few lowest-order Bloch modes in hybrid-clad waveguide as a function of mx and my at a fixed frequency[①] where the group index of the fundamental guided Bloch mode is 5.

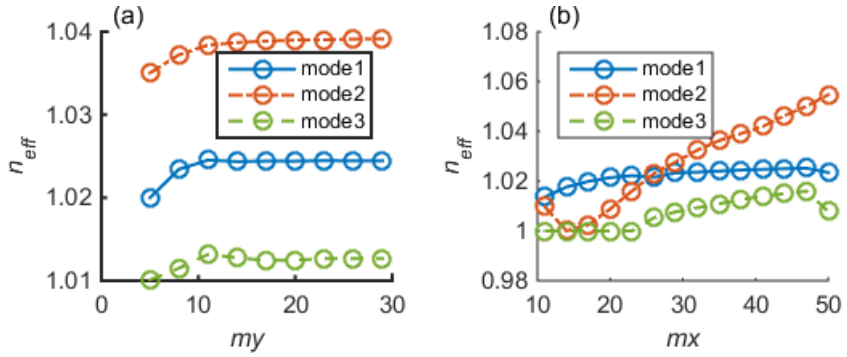

Fig. 5-2. Convergence study of the effective index of the first three lowest-order Bloch modes at wavelength 781 nm (n_g = 5 of the fundamental guided Bloch mode). (a) *mx* = 38 (b) *my* = 29. The blue solid, red dashed and green dash-dotted lines with circles represent the effective index of the first, second and thirst lowest-order modes.

As shown in Fig. 5-2, the mode starts converging for *my* ≥ 14, with a relative error in n_{eff}-value less than 0.1%. We conclude that *my* = 14 is sufficient to get the mode calculation converge. Therefore, *my* = 14 is chosen to save computation time hereafter. In contrast, the n_{eff}-value slowly stabilizes as the spatial Fourier harmonics *mx* is increased. We find that convergence is achieved for a m*y*-value at least five times smaller than the *mx*-value for mode 1. No convergence is observed for the other two modes in terms of *mx*. However, the convergence is guaranteed for all the three modes in terms of *my*. For the fundamental guided Bloch mode, we can consider its effective index asymptotically stabilize to 1.024±0.003.

[①] The frequency is interpolated from the dispersion curve of the fundamental guided Bloch mode, which is calculated at large mx- and my-values. At the frequency where n_g = 5, the fundamental guided Bloch mode is not slow so that it suffers less numerical dispersion as mx- and my-values are changing.

We have shown that it is hard to achieve a very good convergence for the parameter *mx*. In fact, it is easy to understand this difficulty. Since the FMM or a-FMM is based on Fourier series expansion, to achieve the same accuracy the number of Fourier harmonics required rises up as the complexity of the structure (material function and modes profiles) increases. In our case, the complexity in the horizontal *x*-direction is high, and thus we should increase *mx* accordingly. In the beta factor calculation of chapter 4, we choose *mx* = 50 and *my* = 14 for the sake of saving computational time while without losing too much accuracy.

5.2.2 Normalization of the coupling coefficient

The atom-light interaction strength is characterized by the coupling coefficient (denoted by β factor in chapters 3 and 4) which is the fraction of total radiation power channeled into a guided mode,

$$\beta = \frac{P_{\mathrm{M}}}{P_{\mathrm{Total}}}, \tag{5-8}$$

where P_{M} is the radiation power coupled into the guided mode and P_{Total} is the total radiation power. To evaluate P_{M} and P_{Total}, we need to know the field amplitude of the guided Bloch mode and the total field fed by the electric dipole source at source location. They are obtained by solving the Maxwell's equations with Dirac sources. Assume the presence of a point-like electric dipole source $\mathbf{J}\delta(\mathbf{r}-\mathbf{r}_{\mathrm{A}})$, the Maxwell's equations then write as

$$\boldsymbol{\nabla}\times\mathbf{E} = j\omega\boldsymbol{\mu}(\mathbf{r})\mathbf{H}, \tag{5-9}$$

$$\boldsymbol{\nabla}\times\mathbf{H} = -j\omega\boldsymbol{\varepsilon}(\mathbf{r})\mathbf{E} + \mathbf{J}\delta(\mathbf{r}-\mathbf{r}_{\mathrm{A}}). \tag{5-10}$$

The total field, i.e. the solution of the Maxwell's equations (5-9) and (5-10) can be expanded in the quasinormal Bloch modes basis (see details in ref. [Lec07a]) of the source-free Maxwell's equation, with the expansion coefficient of each quasinormal Bloch mode being the excitation coefficient. The total field (see Fig. 5-3) is expanded as

$$\boldsymbol{\Psi} = \sum_{m>0} C_m^{+}\,\boldsymbol{\Phi}^{(m)}\theta(z-z_{\mathrm{A}}) + \sum_{m>0} C_m^{-}\,\boldsymbol{\Phi}^{(-m)}\theta(z_{\mathrm{A}}-z), \tag{5-11}$$

where $\theta(z)$ is the Heaviside step function, z_{A} is the *z*-coordinate of the source location in the propagation direction of the waveguide, $\boldsymbol{\Phi}^{(m)} = \left[\mathbf{E}^{(m)}, \mathbf{H}^{(m)}\right]e^{jk_m z}$ or $\boldsymbol{\Phi}^{(-m)} = \left[\mathbf{E}^{(-m)}, \mathbf{H}^{(-m)}\right]e^{-jk_m z}$ represents the forward-propagating or backward-propagating Bloch mode of the photonic crystal waveguide and C_m^{+} and C_m^{-} denotes the corresponding forward- and backward-propagating modal excitation coefficients.

By applying Lorentz reciprocity theorem to derive the orthogonality of quasinormal Bloch modes, we find that [Lec07a]

$$\begin{cases} C_m^{+} = -\dfrac{\mathbf{E}^{(-m)}(\mathbf{r}_{\mathrm{A}})\cdot\mathbf{J}e^{-jk_m z_{\mathrm{A}}}}{\mathcal{P}^{(m)}} \\ C_m^{-} = -\dfrac{\mathbf{E}^{(m)}(\mathbf{r}_{\mathrm{A}})\cdot\mathbf{J}e^{jk_m z_{\mathrm{A}}}}{\mathcal{P}^{(m)}} \end{cases}, \tag{5-12}$$

where $\mathcal{P}^{(m)} = \iint_z \left(\mathbf{E}^{(-m)}\times\mathbf{H}^{(m)} - \mathbf{E}^{(m)}\times\mathbf{H}^{(-m)}\right) dS_{xy}$ is independent of the cross-section plane. By definition, the radiation power into the guided Bloch mode m reads as,

$$P_{\mathrm{M}} = \oiint \frac{1}{2} Re\left(\tilde{\mathbf{E}}_{\boldsymbol{m}}\times\left[\tilde{\mathbf{H}}_{\boldsymbol{m}}\right]^{*}\right) d\boldsymbol{S}. \tag{5-13}$$

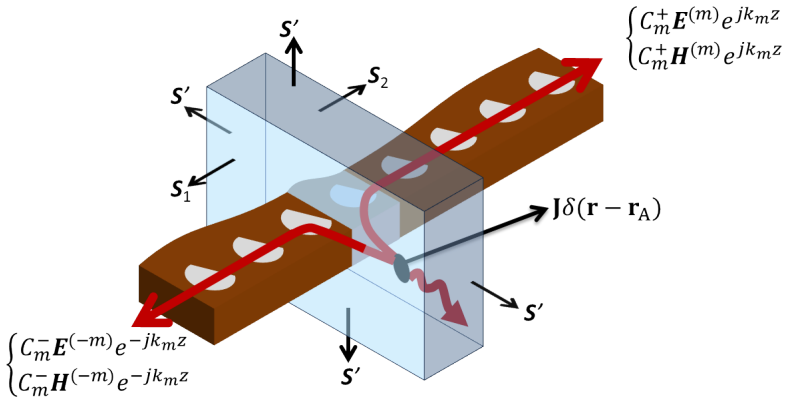

Fig. 5-3. Schematic diagram of the radiation power into the mth mode of a periodic waveguide. A Dirac electric dipole source located at $\boldsymbol{r}_{\mathrm{A}}$ launches light in the (guided and radiation) modes of the waveguide. The computational domain is surunded by the outer-boundary-PML surface S'; two waveguide cross-sections are S_1 and S_2 defined by $z = z_1 < z_{\mathrm{A}}$ and $z = z_2 > z_{\mathrm{A}}$ planes. The red arrows denote the outgoing waves into the mth mode and all the other modes.

We choose the closed surface formed by two waveguide cross-sections, S_1 and S_2 defined by $z = z_1 < z_{\mathrm{A}}$ and $z = z_2 > z_{\mathrm{A}}$, and by the outer-boundary-PML surface S' that closes the two cross-sections. Because of the PML attenuation, the field can be assumed to be negligible on the outer-boundary-PML surface so that the integral on S' is null and the surface integral in Eq. (5-13) reduces to two surface integrals over the cross-section planes S_1 and S_2. Note that for truly guided Bloch modes, we adopt the convention $\left[\mathbf{H}^{(m)}\right]^{*} = -\mathbf{H}^{(-m)}$ (and $\left[\mathbf{E}^{(m)}\right]^{*} = +\mathbf{E}^{(-m)}$) to relate the counter-propagating Bloch modes, and we can express the total power radiated into the mth Bloch mode as

$$P_{\mathrm{M}} = \frac{\mathcal{P}^{(m)}}{4}\left(|C_m^+|^2 + |C_m^-|^2\right). \tag{5-14}$$

Equation (5-14) implies that the quantity P_{M} is independent of the normalization of the quasinormal Bloch modes since both the numerator and denominator contain the same exponent to the field amplitude.

On the other hand, the total radiative power is calculated by

$$P_{\mathrm{Total}} = \frac{1}{2}\mathrm{Re}\left(\mathbf{J}^{*}\cdot\mathbf{E}(\mathbf{r}_{\mathrm{A}})\right). \tag{5-15}$$

Again, the total field at source $\mathbf{E}(\mathbf{r}_{\mathrm{A}})$ that is given by Eq. (3-2) does not depend on the normalization of the quasinormal Bloch modes.

However, the evaluation of the power radiated into mth Bloch mode through Eq. (5-14) involves a surface integral which is not convenient for calculation; the computation of the surface integral requires the knowledge of the field distribution over the whole cross-section, whereas in practice the physical space is bounded by PMLs. Thus the accurate calculation of the integral requires pushing away the PMLs, which is numerically impractical especially if the field expand far away in the clads.

The inconvenience can be avoided by a numerical trick (the "double pepée"), which avoid considering the field in the PML. . Let us denote the normalized mode by $\widehat{\mathbf{\Phi}}^{(m)} = \left[\widehat{\mathbf{E}}^{(m)}, \widehat{\mathbf{H}}^{(m)}\right] e^{jk_m z}$. This field verifies $\iint \widehat{\mathbf{E}}^{(-m)} \times \widehat{\mathbf{H}}^{(m)} - \widehat{\mathbf{E}}^{(m)} \times \widehat{\mathbf{H}}^{(-m)} dS_{xy} = 4$, i.e. the power carried by the normalized guided Bloch mode is 1). Conversely let us denote by $\mathbf{\Phi}^{(m)} = \left[\mathbf{E}^{(m)}, \mathbf{H}^{(m)}\right] e^{jk_m z}$ the non- normalized modes calculated by the eigensolver, and by α the complex coefficient such that $\mathbf{\Phi}^{(m)} = \alpha \widehat{\mathbf{\Phi}}^{(m)}$. Then, the objective is to calculate α.

For that purpose, we solve the radiation problem of a Dirac dipole source located at $\mathbf{r}_\mathrm{A}$ in a periodic waveguide with a-FMM Bloch method [Lec07a], and compute the excitation coefficient C_m^+ of the mth Bloch mode (not normalized). The computed coefficient is given by Eq. (5-12). Since $\mathbf{\Phi}^{(m)} = \alpha \widehat{\mathbf{\Phi}}^{(m)}$, we have $\mathcal{P}^{(m)} = 4|\alpha|^2$. Therefore,

$$|\alpha|^2 = -\frac{\mathbf{E}^{(-m)}(\mathbf{r}_\mathrm{A}) \cdot \mathbf{J} e^{-jk_m z_\mathrm{A}}}{C_m^+} \tag{5-16}$$

can be calculated as a function of $\mathbf{J}$, $\mathbf{E}^{(-m)}(\mathbf{r}_\mathrm{A})$, $e^{-jk_m z_\mathrm{A}}$ and C_m^+ that are all available from the Bloch-modal method.

To summarize, with the "double pesée", one avoids the necessity of pushing away the PML by solving an emission problem in the presence of the PML. A priori, any Dirac source might be used, but we will see that magnetic-dipole sources provide better accuracy for computing α with a-FMM.

5.2.3 Accuracy of the normalization coefficient

The normalization coefficient should be independent of the location or polarization of the inserted Dirac dipole source. Numerically, however, we find that the normalization coefficient α does depend on source locations and polarizations, as presented in Fig. 5-4.

The accuracy of normalization coefficient obtained from H_y-polarized dipole source is obviously much higher than that obtained from other polarizations. For this reason, it is much more accurate to normalize the modal field by the normalization coefficient α obtained from H_y-polarized source, denoted by $\alpha_{Hy}(x)$. Furthermore, we average $\alpha_{Hy}(x)$ over x in order to lower numerical errors[②]. Then, the normalized modal field can be obtained through the relation $\mathbf{\Phi}^{(m)} = \alpha_{Hy} \widehat{\mathbf{\Phi}}^{(m)}$, with $\alpha_{Hy} = <\alpha_{Hy}(x)>$.

[②]The relative errors of α_{Hy} in both y-direction and z-direction are expected to be less than 1% which is negligible as well.

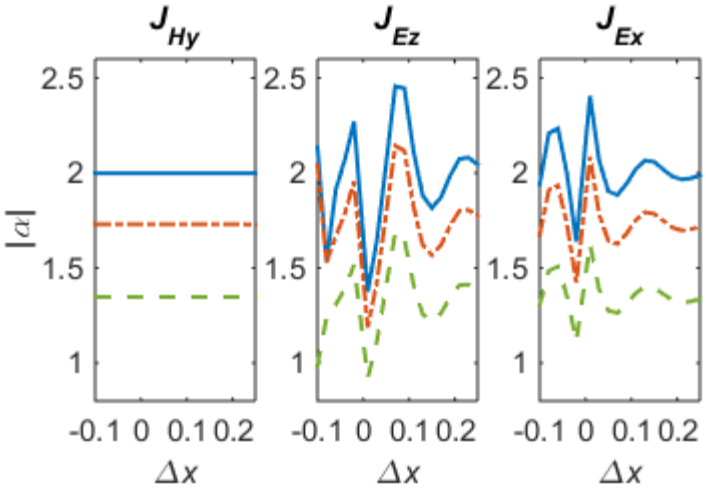

Fig. 5-4. The normalization coefficient, $|\alpha|$ as a function of the dipole source location along the transverse direction x for three polarized dipole sources: (left) H_y-polarized dipole, (middle) E_z-polarized dipole and (right) E_x-polarized dipole. Each group of lines are plotted for n_g = 5, 10, 50 indicated by blue solid, red dash-dotted and green dashed lines, respectively.

5.2.4 Convergence of the reflection coefficient

Here, we study the accuracy of the all the numerical results shown in chapters 3 and 4 for the reflectance of a single atom, and show that the numerical results are accurate enough so that all the discussion and conclusion are valid.

a. Hybrid-clad waveguide

The convergence tests performed for the hybrid-clad waveguide (chapter 4) are summarized in Fig. 5-5. We took the numerical dispersion into account, i.e. we recalculate the dispersion curve of the fundamental guided Bloch mode while the number of spatial Fourier harmonics varies from 15 to 50.

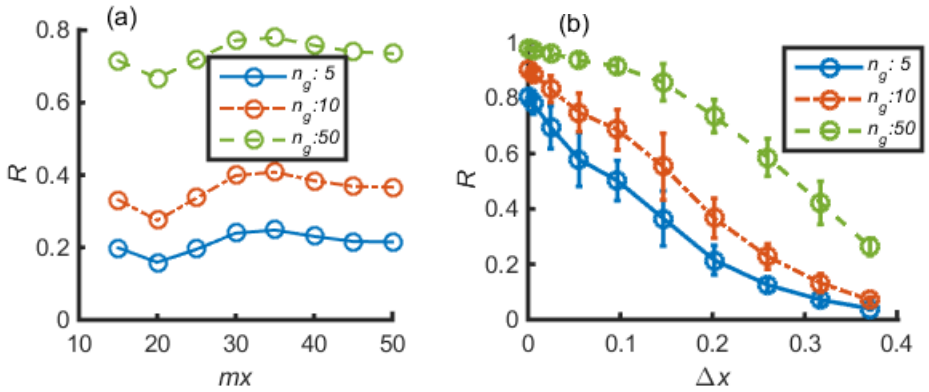

Fig. 5-5. Accuracy of reflectance of the fundamental guided Bloch mode by a single cold atom. (a) Convergence of the reflectance for n_g = 5 (blue solid line with circles), n_g = 10 (red dash-dotted) and 50 (green dash) for an atom positioned at a distance of 200 nm from the waveguide sidewall. (b) The reflection along the cross line of two high symmetric planes for mx = 50. The

solid blue, red and green lines represent the reflectance for n_g = 5, 10, 50 separately. The vertical bars indicate the maximum difference among the reflectance obtained for *mx* = 25, 30, 35, 40, 45 and 50.

b. Sub-wavelength periodic nanowire

The main result in chapter 3 is the reflectance of the incident guided Bloch mode by a single atom located in the air-gap of a waveguide composed of an array of semiconductor boxes. Fig. 5-6 summarizes the numerical accuracy tests.

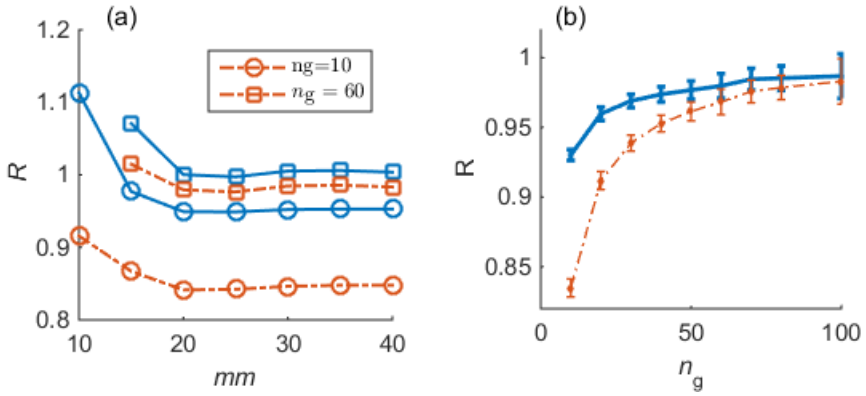

Fig. 5-6. Numerical accuracy of reflectance of a single atom in sub-wavelength periodic nanowire. (a) Convergence of the rigorous and approximated reflectance for n_g = 10 (circles) and 60 (squares). For both n_g-values, the blue solid lines represent the rigorous reflectance and the red dash-dotted lines give the corresponding approximated values. (b) Reflectance varies as a function of n_g for *mm* = 40. The blue solid line shows the rigorously calculated reflectance, and the red dash-dotted line represents the results obtained through the approximate treatment. The vertical bars are defined as in the caption of Fig. 5-5.

The lengths of the vertical bars indicate that the accuracy of both the rigorous and approximate values decreases as the group index increases. We found that the numerical results stabilize for *mm* > 20 with the uncertainty less than 0.5% for n_g = 10 and 2% for n_g = 100. At last, we additionally note the difference between the approximate and rigorous reflectances reduce as the group index increases.

5.2.5 Convergence of the β factor

For the normalized mode, the accuracy of the reflection coefficient, which is given by Eq. (3-7) in chapter 3, is totally determined by the β factor of the fundamental guided Bloch mode. The β factor is defined as the ratio of P_M to P_{Total}, where the quantity P_{Total} is the sum of P_M and P_γ, P_M being the power radiated into the guided mode and P_γ the power radiated into all the other modes. Therefore, the β factor is finally affected by two quantities, P_M and P_γ. In the following section, for the sake of illustration, we show how the mode confinement affects the convergence rate of these two quantities in a simple ridge waveguide.

Radiation in a Ridge waveguide

We study the numerical accuracy of the power radiation into a guided mode P_M and the

power radiated into all the other modes P_γ, which might include a few guided modes and the continuum. The schematic diagram of Dirac dipole radiation in a ridge waveguide is shown in Fig. 5-7. Hereafter all powers are normalized by the power radiation in a bulk material with refractive index of 3.5.

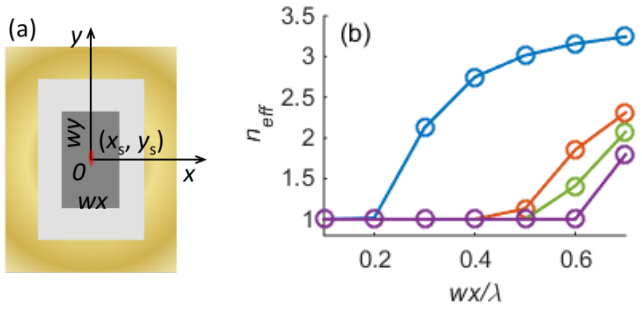

Fig. 5-7. Schematic diagram of the Dirac dipole radiation at λ = 1.5 μm in a *z-invariant* ridge waveguide. (a) The red solid ellipse indicates the Dirac dipole at position (x_s, y_s). (a) The outer yellow box represents the PML layer with thickness 1.5 μm in x and y directions. The ridge waveguide has a size of $wx \times wy$ and a refractive index of 3.5. (b) The effective index of the first 4 lowest order guided modes that are symmetric along both x and y directions as a function of wx/λ.

In the following simulations, we maintain the ratio of *wy/wx* to be 1.1 so that the degeneracy of the modes is removed. The vacuum cladding thickness is set to be 0 μm, i.e. the PML layers touch the boundary of the ridge waveguide. The fundamental guided mode has a dominant E_y field component. We first calculated the coupling between a Dirac electric dipole source with E_y-polarization located in the center at (x_s, y_s) = (0, 0), and the fundamental guided mode.

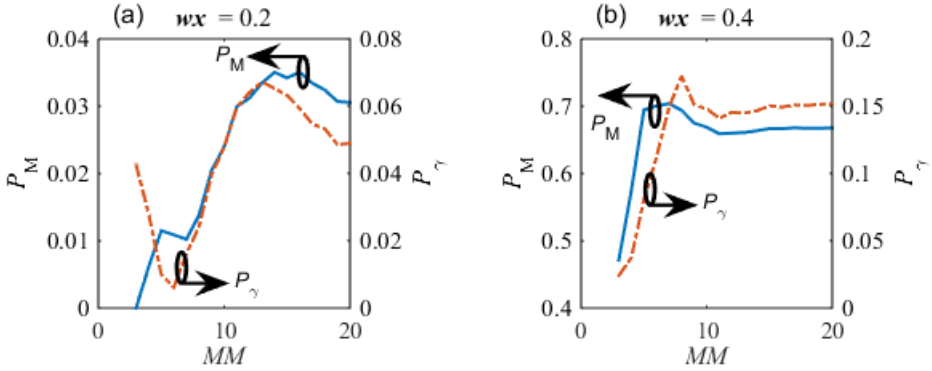

Fig. 5-8. Convergence of the radiation power, P_M into the guided mode, and P_γ into all the other modes. The powers are normalized to the power radiation in a bulk material with refractive index of 3.5. (a) The ridge waveguide has a size of $wx \times wy$ = 0.2 × 0.22 μm². (b) The ridge waveguide has a size of $wx \times wy$ = 0.4 × 0.44 μm². The blue solid line represents P_M. The red dash-dotted curve represents P_γ.

For tiny ridge waveguide, Fig. 5-8(a), the fundamental guided mode is weakly confined. The E_y-polarized Dirac electric dipole only weakly couples to the fundamental guided mode and P_M

< 0.04; it couples even more into all the other modes. On the other hand, when the E_y-polarized Dirac electric dipole radiates in a large ridge waveguide (Fig. 5-8(b)), the coupling ~0.67 into the fundamental guided mode dominates while P_γ remains smaller than 0.15. In terms of convergence performance, the quantities P_{M} and P_γ converge quickly to 0.67 and 0.15 separately when the fundamental guided mode is well confined, as shown in Fig. 5-8(b), while these two quantities vary a lot in the case of a weak confinement, as shown in Fig. 5-8(a).

This might explain the numerical difficulties encountered in chapter 4 with the hybrid-cladd waveguide. In comparison, for a related photonic-crystal waveguide problem, excellent accuracy was achieved for calculating the β factor in 2007 with the a-FMM [Lec07a], but the source was inside the waveguide and was very well coupled to the guided mode.

5.3 Conclusion and perspectives

In this chapter, we firstly described the numerical method used throughout the thesis. In section 5.2, we have explained why and how we normalize the guided Bloch mode. In addition, we have analyzed the accuracy of the reflection coefficient and coupling coefficient. The effect of the mode confinement on the accuracy of the coupling coefficient has also been articulated. For the application of slow light in air, the mode is potentially weakly confinement, and the accuracy of the coupling coefficient is low. To reach high precision in numerical simulations, one must take additional effort to optimize several key numerical parameters, e.g. PMLs, adaptive spatial resolution and cladding air thickness etc., which is beyond the scope of this thesis. The approximation method developed here allows us to discuss physical trends with reliable conclusions.

The aperiodic-Fourier modal method is efficient for analyzing the nanostructures that are translational invariant or periodic in at least one direction, since it avoids spatial discretization on this direction. Even for photonic crystal waveguide, the Fourier modal method still overwhelms, in term of computational time, many numerical simulation methods that rely on fully spatial discretization. However, two difficulties arise for the hybrid-clad waveguide. First, the computational window is large so that potentially more spatial Fourier harmonics is required; second, the guided mode is weakly confined thus the field extends far away into the cladding air region, which in turn requires even larger computational window. We have found that rigorously calculating the coupling coefficient of the single atom to the guided Bloch mode requires complex numerical optimization. Rather than fully tackling these issues, we have carefully developed an approximation treatment so that we are able to get good accuracies without performing complex numerical simulations. The approximation treatment only relies on the accurate calculation of the fundamental guided Bloch mode and of its normalization which not only circumvents the simulation complexity but also provides a convenient tool for quickly characterizing the light scattering of a single atom in nanophotonic environment. The approximation treatment is also compared with the rigorous calculation in a simple Pavel waveguide as shown in section 5.2.4.

There are several possibilities to improve the numerical accuracy. Firstly, we have just implemented the adaptive spatial resolution method only for the sub-wavelength periodic nanowire and the related parameters are not optimized. To reach higher precision, we can optimize the adaptive spatial resolution. Secondly, we could have rigorously calculated the

coupling coefficient provided that the numerical parameters were well chosen. It is also possible to use other numerical tools, e.g. finite element method that is more suitable for handling intrinsic discontinuities of the structure and field components.

6 Conclusions and Perspectives

With the objective of reinforcing light-matter interaction by implementing slow light in photonic crystal waveguides, in this thesis, we have studied light localization in real photonic crystal waveguides and scattering properties of single atoms near periodic waveguides, and we have proposed a novel design that bears large coupling between cold atoms and photonic crystal waveguides.

In chapter 2, we have studied the relation between light localization and disorder level in slow light photonic devices. Firstly, the existence of localized modes in photonic crystal waveguides that are fabricated without any intentional disorder has been attested experimentally through near-field measurements. Furthermore, we have performed statistical calculations that reveal a lower bound exists in the localized mode size, i.e. the extension of the localized modes cannot be smaller than a certain value for a certain photonic structure at a given disorder level. In addition, we have evidenced by a simple model that the bound is related to the effective photon mass (the curvature of the dispersion curve) rather than the group index, which is somewhat counterintuitive with respect to the previous studies.

Our findings might be instructive for photonic devices design in which disorder becomes a stringent limitation on the functionalities of the photonic devices. For example, light localization can be well harnessed to enhance the devices performance for applications in biological imaging, random lasing and solar energy [Wie13]. On the other hand, for applications in hybrid cold atoms and nanophotonics systems where light localization potentially deteriorate the functionality of the systems [Gob14] even with state-of-the-art fabrication technology, disorder induced localization should be carefully avoided. In any case, we hope our study will help for future high-performance and robust designs. From the point of view of fundamental physics, our emphasis on the curvature of the dispersion curve, i.e. the effective photon mass, may inspire the conceptual understanding of Anderson localization in disordered media.

In chapter 3, we have studied the scattering properties of guided photons by one atom. We have derived a semi-analytical expression for analyzing the scattering of guided photons by cold atoms trapped near periodic waveguides. To our knowledge, so far, only ref. [Hun13] considers the interaction of an atom with a periodic waveguide in the slow light regime, with a fully numerical method (FDTD) followed by Fourier analysis. Our derived semi-analytical modal formalisms are, however, advantageous since the modal formalisms are directly expressed into quasinormal Bloch mode basis and Bloch mode formalisms have been shown high flexibility for studying light propagation and scattering in the context of light localization in photonic crystal waveguides [Lec07b; Sau05a; Bar11].

Our theoretical treatment of the scattering matrix of one atom [She05] represents an extension of previous work. Firstly, the phase of transmitted and reflected photons, the saturation of the atom for multiphoton incident states and radiation due to imperfect atom-waveguide coupling can be accurately taken into account. Moreover, Bloch-mode scattering matrix of single atoms is an building block to analysis of collective effects [Gob15] of a chain of trapped atoms along periodic waveguides. Furthermore, the approximation provides

great flexibility to deeply understand and quickly characterize the optical responses when some physical parameters are tuned, such as the group velocity or the atom positions. Last, our modal formalism is general since it applies to atom-field interactions that are mediated not only by propagative photons in the band, but also for photons with energies within the gap.

In the emerging field of on-chip integration of nanophotonic devices and cold atoms, indeed there are many challenges including atom loading, light scattering from device imperfections, atom-photon resonance matching, robustness against vacuum-force fluctuations, in spite of the profound impact on all-optical information processing and quantum information science it may bring. In chapter 4, we have proposed a novel slow-light waveguide geometry that tends to achieve large couplings between single atoms and single photons, for atoms that are trapped at large separation distances from dielectric walls of the waveguide.

Large coupling between trapped atoms and guided mode is driven by efficient light slowdown and the enhancement of field intensity felt by cold atoms. However, they are two contradictory efforts, i.e. engineering efficient slow light and extracting intense evanescent tail far in the vacuum cladding where the atoms are loaded and feel negligible/weak Casmir-Polder forces. Therefore, a best design is devoted to compromise between light slowdown and light extraction. The present design directly addresses the conflict and represents a relatively compromised solution. Moreover, with respect to the trapping of cold atoms, it decouples the trapping and atom-field-interaction problems and offers a 2π solid-angle access to the interaction region, allowing for "easy" manipulations of atomic clouds around the structure by other external standing waves. Last, the engineered dispersion curve of the proposed waveguide, because it possesses large effective photon masses (in comparison to earlier works [Gob14]), offers a robust design and allows us to precisely match the atomic transition and the slow light frequencies.

In chapter 5 we have studied the convergence performance of the numerical software that was used in the thesis to predict some key quantities characterizing atom-field interaction. Furthermore, the numerical techniques described in this chapter, e.g. the normalization approach, can be practically useful for theoretical studies of light-matter interactions in hybrid cold atoms and nanophotonics systems.

Perspectives

Limited by the finite duration of PhD study, I couldn't finish all the work especially the one in chapter 4. Here, I address some directions that could be worked on in the near future.

In the theoretical proposal of chapter 4, we haven't explicitly addressed and discussed the trapping of cold atoms in the vicinity of waveguides. As far as we know, the external light beam can be implemented to form standing waves and can be utilized for trapping cold atoms [Tho13]. In this configuration, the minimum trap distance is limited to about 100 nm [Tho13] due to attractive van der Waals interaction between the atom and the surface. We can study the surface attractive force and optical dipole forces exerted by the dielectric structure and external standing waves.

Alternatively, a second guided mode at large detuning can be implemented for trapping like the method used in [Hun13]. However, our novel geometry is more complicated than the slotted

quasi one-dimensional photonic crystal waveguide [Hun13], thus the design of such a guided mode for trapping is not easy since it involves optimizing many geometric parameters. Anyway, this work is quite exciting and worth trying. Rather than utilizing guided modes, it is also possible to implement Bloch surface eigenstates within the radiation continuum [Wei13]. Such Bloch surface eigenstates is topologically robust against fabrication imperfections. In addition, since the frequency of the trapping field does not have to match precisely a certain value, the frequency drift that arises from disorder, can be easily compensated by modifying the intensity of the trapping field.

Lists of Publications

This thesis is based on the following publications:

Stepanov P, Delga A, Zang X, Bleuse J, Dupuy E, Peinke E, Lalanne P, Gérard J-M, Claudon J (2015) Quantum dot spontaneous emission control in a ridge waveguide. Appl. Phys. Lett. 106:041112. doi: 10.1063/1.4906921 . (**Chapter 5**)

Faggiani R, Baron A, Zang X, Lalouat L, Schulz SA, Vynck K, O'Regan B, Cluzel B, de Fornel F, Krauss TF, Lalanne P (2015) Ultimate limits of light confinement in randomly-perturbed periodic structures. arXiv:1505.03472 [physics.optics] (**Chapter 2**)

Zang X, Lalanne P (2015) Theoretical treatment of the interaction between two-level atoms and periodic waveguides. arXiv:1506.01176 [physics.optics] (**Chapter 3**)

Zang X, Yang J, Faggiani R, Gill C, Petrov PG, Bernon S, Bouyer P, Boyer V, Lalanne P (2015) Interaction between atoms and slow light : a design study. in preparation. (**Chapter 4**)

Part of the work has also been presented in conferences:

Zang X, Lalanne P (2013) Strong localization in unintentional disordered photonics crystal waveguides. 2013 7th Int Congr Adv Electromagn Mater Microwaves Opt METAMATERIALS 2013 322–324. doi: 10.1109/MetaMaterials.2013.6809040

Baron A, Faggiani R, Zang X, Lalouat L, Schulz SA, Vynck K, et al. «Localization of Light at Vanishingly Small Disorder-Levels with Heavy Photons». CLEO:QELS Fundamental Science, Paper #FW1C.4, San Jose, CA, USA (2015)

Baron A, Faggiani R, Zang X, Lalouat L, Schulz SA, Vynck K, et al. «Heavy Photons for Light Localization at Vanishingly Small Disorder-Levels», CLEO/Europe 2015, Paper #CK-11.1, Munich, Germany (2015)

Bibliography

[And58] Anderson, P.W., 1958. Absence of Diffusion in Certain Random Lattices. *Physical Review*, 109(5), pp.1492–1505.

[And85] Anderson, P.W., 1985. The question of classical localization A theory of white paint? *Philosophical Magazine Part B*, 52(3), pp.505–509.

[Bab08] Baba, T., 2008. Slow light in photonic crystals. *Nature Photonics*, 2(8), pp.465–473.

[Bar00] Barnett, A.H. et al., 2000. Substrate-based atom waveguide using guided two-color evanescent light fields. *Physical Review A*, 61(2), p.023608.

[Bar07] Barth, M. et al., 2007. Modification of visible spontaneous emission with silicon nitride photonic crystal nanocavities. *Optics Express*, 15(25), p.17231.

[Bar08] Barth, M. et al., 2008. Emission properties of high-Q silicon nitride photonic crystal heterostructure cavities. *Applied Physics Letters*, 93(2), p.021112.

[Bar11] Baron, A. et al., 2011. Attenuation Coefficient of Single-Mode Periodic Waveguides. *Physical Review Letters*, 107(15), p.153901.

[Bes07] Besbes, M. et al., 2007. Numerical analysis of a slit-groove diffraction problem. *Journal of the European Optical Society: Rapid Publications*, 2, p.07022.

[Bil08] Billy, J. et al., 2008. Direct observation of Anderson localization of matter waves in a controlled disorder. *Nature*, 453(7197), pp.891–4.

[Boy11] Boyd, R.W., 2011. Material slow light and structural slow light: similarities and differences for nonlinear optics [Invited]. *Journal of the Optical Society of America B*, 28(12), p.A38.

[Caz13] Cazé, A. et al., 2013. Strong Coupling to Two-Dimensional Anderson Localized Modes. *Physical Review Letters*, 111(5), p.053901.

[Cha07] Chang, D.E. et al., 2007. A single-photon transistor using nanoscale surface plasmons. *Nature Physics*, 3(11), p.807.

[Cha11] Chang, Y. et al., 2011. Multiatomic mirror for perfect reflection of single photons in a wide band of frequency. *Physical Review A*, 83(1), p.013825.

[Che13] Chen, X.-W. et al., 2013. Coherent Interaction of Light with a Metallic Structure Coupled to a Single Quantum Emitter: From Superabsorption to Cloaking. *Physical Review Letters*, 110(15), p.153605.

[Che94] Chew, W.C. & Weedon, W.H., 1994. A 3D perfectly matched medium from modified maxwell's equations with stretched coordinates. *Microwave and Optical Technology Letters*, 7(13), pp.599–604.

[Cot72] Cottey, A.A., 1972. Solutions of Schrodinger's equation at a band edge in a one dimensional crystal. *Journal of Physics C: Solid State Physics*, 5(18), pp.2583–2590.

[Dal91] Dalichaouch, R. et al., 1991. Microwave localization by two-dimensional random scattering. *Nature*, 354(6348), pp.53–55.

[Del12] Dellinger, J. et al., 2012. Hyperspectral optical near-field imaging: Looking graded photonic crystals and photonic metamaterials in color. *Applied Physics Letters*, 101(14), p.141108.

[Dou15] Douglas, J.S. et al., 2015. Quantum many-body models with cold atoms coupled to photonic crystals. *Nature Photonics*, advance on.

[Fag15] Faggiani, R. et al., 2015. Ultimate limits of light confinement in randomly-perturbed periodic structures. *arXiv:1505.03472*.

[Fra06] Frandsen, L.H. et al., 2006. Photonic crystal waveguides with semi-slow light and tailored dispersion properties. *Optics Express*, 14(20), p.9444.

[Gao13] Gao, J. et al., 2013. Strongly coupled slow-light polaritons in one-dimensional disordered localized states. *Scientific reports*, 3, p.1994.

[Gob14] Goban, A. et al., 2014. Atom-light interactions in photonic crystals. *Nature communications*, 5, p.3808.

[Gob15] Goban, A. et al., 2015. Superradiance for atoms trapped along a photonic crystal waveguide. *arXiv:1503.04503*.

[Gon11] Gonzalez-Tudela, A. et al., 2011. Entanglement of Two Qubits Mediated by One-Dimensional Plasmonic Waveguides. *Physical Review Letters*, 106(2), p.020501.

[Gra96] Granet, G. & Guizal, B., 1996. Efficient implementation of the coupled-wave method for metallic lamellar gratings in TM polarization. *Journal of the Optical Society of America A*, 13(5), p.1019.

[Gry10] Grynberg, G. et al., 2010. *Introduction to Quantum Optics: From the Semi-classical Approach to Quantized Light*, Cambridge University Press.

[Hal15] Halir, R. et al., 2015. Waveguide sub-wavelength structures: a review of principles and applications. *Laser & Photonics Reviews*, 9(1), p.25.

[Hug05a] Hughes, S. et al., 2005. Extrinsic Optical Scattering Loss in Photonic Crystal Waveguides: Role of Fabrication Disorder and Photon Group Velocity. *Physical Review Letters*, 94(3), p.033903.

[Hug05b] Hugonin, J.P. & Lalanne, P., 2005. Perfectly matched layers as nonlinear coordinate transforms: a generalized formalization. *Journal of the Optical Society of America A*, 22(9), p.1844.

[Hui12] Huisman, S.R. et al., 2012. Measurement of a band-edge tail in the density of states of a photonic-crystal waveguide. *Physical Review B*, 86(15), p.155154.

[Hun13] Hung, C.-L. et al., 2013. Trapped atoms in one-dimensional photonic crystals. *New Journal of Physics*, 15(8), p.083026.

[Ike08] Ikeda, K. et al., 2008. Thermal and Kerr nonlinear properties of plasma-deposited silicon nitride/ silicon dioxide waveguides. *Optics Express*, 16(17), p.12987.

[Izr09] Izrailev, F. & Makarov, N., 2009. Localization in Correlated Bilayer Structures: From Photonic Crystals to Metamaterials and Semiconductor Superlattices. *Physical Review Letters*, 102(20), p.203901.

[Joh01] Johnson, S. & Joannopoulos, J., 2001. Block-iterative frequency-domain methods for Maxwell's equations in a planewave basis. *Optics Express*, 8(3), p.173.

[Joh84] John, S., 1984. Electromagnetic Absorption in a Disordered Medium near a Photon Mobility Edge. *Physical Review Letters*, 53(22), pp.2169–2172.

[Joh87] John, S., 1987. Strong localization of photons in certain disordered dielectric superlattices. *Physical Review Letters*, 58(23), pp.2486–2489.

[Joh91] John, S., 1991. Localization of Light. *Physics Today*, 44(5), p.32.

[Kal06] Kaliteevski, M. et al., 2006. Statistics of the eigenmodes and optical properties of one-dimensional disordered photonic crystals. *Physical Review E*, 73(5), p.056616.

[Kie04] Le Kien, F. et al., 2004. Atom trap and waveguide using a two-color evanescent light field around a subwavelength-diameter optical fiber. *Physical Review A*, 70(6), p.063403.

[Kie05] Le Kien, F. et al., 2005. Spontaneous emission of a cesium atom near a nanofiber: Efficient coupling of light to guided modes. *Physical Review A*, 72(3), p.032509.

[Koe05] Koenderink, A. et al., 2005. Controlling the Resonance of a Photonic Crystal Microcavity by a Near-Field Probe. *Physical Review Letters*, 95(15), p.153904.

[Koj03] Kojima, K. et al., 2003. Nonlinear interaction of two photons with a one-dimensional atom: Spatiotemporal quantum coherence in the emitted field. *Physical Review A*, 68(1), p.013803.

[Lag09] Lagendijk, A. et al., 2009. Fifty years of Anderson localization. *Physics Today*, 62(8), pp.24–29.

[Lal00] Lalanne, P. & Silberstein, E., 2000. Fourier-modal methods applied to waveguide computational problems. *Optics Letters*, 25(15), p.1092.

[Lal02] Lalanne, P., 2002. Electromagnetic analysis of photonic crystal waveguides operating above the light cone. *IEEE Journal of Quantum Electronics*, 38(7), pp.800–804.

[Lal08] Lalanne, P. et al., 2008. Photon confinement in photonic crystal nanocavities. *Laser & Photonics Review*, 2(6), pp.514–526.

[Lal96] Lalanne, P. & Morris, G.M., 1996. Highly improved convergence of the coupled-wave method for TM polarization. *Journal of the Optical Society of America A*, 13(4), p.779.

[Lal98] Lalanne, P., 1998. Effective properties and band structures of lamellar subwavelength crystals: Plane-wave method revisited. *Physical Review B*, 58(15), pp.9801–9807.

[Lec07a] Lecamp, G. et al., 2007. Theoretical and computational concepts for periodic optical waveguides. *Optics Express*, 15(18), p.11042.

[Lec07b] Lecamp, G. et al., 2007. Very Large Spontaneous-Emission β Factors in Photonic-Crystal Waveguides. *Physical Review Letters*, 99(2), p.023902.

[Lev09] Levy, J.S. et al., 2009. CMOS-compatible multiple-wavelength oscillator for on-chip optical interconnects. *Nature Photonics*, 4(1), pp.37–40.

[Li93] Li, L. & Haggans, C.W., 1993. Convergence of the coupled-wave method for metallic lamellar diffraction gratings. *Journal of the Optical Society of America A*, 10(6), p.1184.

[Li96a] Li, L., 1996. Formulation and comparison of two recursive matrix algorithms for modeling layered diffraction gratings. *Journal of the Optical Society of America A*, 13(5), p.1024.

[Li96b] Li, L., 1996. Use of Fourier series in the analysis of discontinuous periodic structures. *Journal of the Optical Society of America A*, 13(9), p.1870.

[Li97] Li, L., 1997. New formulation of the Fourier modal method for crossed surface-relief gratings. *Journal of the Optical Society of America A*, 14(10), p.2758.

[Lod15] Lodahl, P. et al., 2015. Interfacing single photons and single quantum dots with photonic nanostructures. *Reviews of Modern Physics*, 87(2), pp.347–400.

[Lun08] Lund-Hansen, T. et al., 2008. Experimental Realization of Highly Efficient Broadband Coupling of Single Quantum Dots to a Photonic Crystal Waveguide. *Physical Review Letters*, 101(11), p.113903.

[Mai03] Maier, S.A. et al., 2003. Local detection of electromagnetic energy transport below the diffraction limit in metal nanoparticle plasmon waveguides. *Nature materials*, 2(4), p.229.

[Mak06] Makarova, M. et al., 2006. Silicon-based photonic crystal nanocavity light emitters. *Applied Physics Letters*, 89(22), p.221101.

[Man07] Managa Rao, V.S.C. & Hughes, S., 2007. Single quantum dots for slow and fast light in a planar photonic crystal. *Optics Letters*, 32(3), p.304.

[Maz09] Mazoyer, S. et al., 2009. Disorder-Induced Multiple Scattering in Photonic-Crystal Waveguides. *Physical Review Letters*, 103(6), p.063903.

[Maz10] Mazoyer, S. et al., 2010. Statistical fluctuations of transmission in slow light photonic-crystal waveguides. *Optics Express*, 18(14), p.14654.

[Mel14] Melati, D. et al., 2014. Real photonic waveguides: guiding light through imperfections. *Advances in Optics and Photonics*, 6(2), p.156.

[Moh81] Moharam, M.G. & Gaylord, T.K., 1981. Rigorous coupled-wave analysis of planar-grating diffraction. *Journal of the Optical Society of America*, 71(7), p.811.

[Moh95] Moharam, M.G. et al., 1995. Formulation for stable and efficient implementation of the rigorous coupled-wave analysis of binary gratings. *Journal of the Optical Society of America A*, 12(5), p.1068.

[Moo08] Mookherjea, S. et al., 2008. Localization in silicon nanophotonic slow-light waveguides. *Nature Photonics*, 2(2), pp.90–93.

[Mor05] Mori, D. & Baba, T., 2005. Wideband and low dispersion slow light by chirped photonic crystal coupled waveguide. *Optics Express*, 13(23), p.9398.

[Mot49] Mott, N.F., 1949. The Basis of the Electron Theory of Metals, with Special Reference to the Transition Metals. *Proceedings of the Physical Society. Section A*, 62(7), pp.416–422.

[Muj07] Mujumdar, S. et al., 2007. Near-field imaging and frequency tuning of a high-Q photonic crystal membrane microcavity. *Optics Express*, 15(25), p.17214.

[Net00] Netti, M.C. et al., 2000. Visible photonic band gap engineering in silicon nitride waveguides. *Applied Physics Letters*, 76(8), p.991.

[Not01] Notomi, M. et al., 2001. Extremely Large Group-Velocity Dispersion of Line-Defect Waveguides in Photonic Crystal Slabs. *Physical Review Letters*, 87(25), p.253902.

[Not10] Notomi, M., 2010. Manipulating light with strongly modulated photonic crystals. *Reports on Progress in Physics*, 73(9), p.096501.

[Pat09] Patterson, M. et al., 2009. Disorder-Induced Coherent Scattering in Slow-Light Photonic Crystal Waveguides. *Physical Review Letters*, 102(25), p.253903.

[Pet04] Petrov, A.Y. & Eich, M., 2004. Zero dispersion at small group velocities in photonic crystal waveguides. *Applied Physics Letters*, 85(21), p.4866.

[Pis03] Pissoort, D. & Olyslager, F., 2003. Termination of periodic waveguides by PMLs in time-harmonic integral equation-like techniques. *IEEE Antennas and Wireless Propagation Letters*, 2(1), p.281.

[Pod12] Poddubny, A.N. et al., 2012. Fano interference governs wave transport in disordered systems. *Nature communications*, 3, p.914.

[Pop00] Popov, E. & Nevière, M., 2000. Grating theory: new equations in Fourier space leading to fast converging results for TM polarization. *Journal of the Optical Society of America A*, 17(10), p.1773.

[Por11] Portalupi, S.L. et al., 2011. Deliberate versus intrinsic disorder in photonic crystal nanocavities investigated by resonant light scattering. *Physical Review B*, 84(4), p.045423.

[Red13] Redding, B. et al., 2013. Compact spectrometer based on a disordered photonic chip. *Nature Photonics*, 7(9), pp.746–751.

[Roa08] Roati, G. et al., 2008. Anderson localization of a non-interacting Bose-Einstein condensate. *Nature*, 453(7197), pp.895–8.

[Sac95] Sacks, Z.S. et al., 1995. A perfectly matched anisotropic absorber for use as an absorbing boundary condition. *IEEE Transactions on Antennas and Propagation*, 43(12), pp.1460–1463.

[Sap10] Sapienza, L. et al., 2010. Cavity quantum electrodynamics with Anderson-localized modes. *Science (New York, N.Y.)*, 327(5971), pp.1352–5.

[Sau05a] Sauvan, C. et al., 2005. Slow-wave effect and mode-profile matching in photonic crystal microcavities. *Physical Review B*, 71(16), p.165118.

[Sau05b] Sauvan, C. & Lalanne, P., 2005. Comment on "Anomalous Propagation Loss in Photonic Crystal Waveguides." *Physical Review Letters*, 95(22), p.229401.

[Scu13] Scullion, M.G. et al., 2013. Slotted photonic crystal sensors. *Sensors (Basel, Switzerland)*, 13(3), pp.3675–710.

[Seb06] Sebbah, P. et al., 2006. Extended Quasimodes within Nominally Localized Random Waveguides. *Physical Review Letters*, 96(18), p.183902.

[She05] Shen, J.T. & Fan, S., 2005. Coherent photon transport from spontaneous emission in one-dimensional waveguides. *Optics Letters*, 30(15), p.2001.

[Sil01] Silberstein, E. et al., 2001. Use of grating theories in integrated optics. *Journal of the Optical Society of America A*, 18(11), p.2865.

[Sny84] Snyder, A.W. & Love, J.D., 1984. *Optical Waveguide Theory*, Boston, MA: Springer US.

[Sol04] SoljaČiĆ, M. & Joannopoulos, J.D., 2004. Enhancement of nonlinear effects using photonic crystals. *Nature Materials*, 3(4), pp.211–219.

[Son05] Song, B.-S. et al., 2005. Ultra-high-Q photonic double-heterostructure nanocavity. *Nature Materials*, 4(3), pp.207–210.

[Spe13] Sperling, T. et al., 2013. Direct determination of the transition to localization of light in three dimensions. *Nature Photonics*, 7(1), pp.48–52.

[Ste10] Steck, D.A., 2010. *"Cesium D Line Data,"* Los Alamos National Laboratory (unpublished).

[Stö06] Störzer, M. et al., 2006. Observation of the Critical Regime Near Anderson Localization of Light. *Physical Review Letters*, 96(6), p.063904.

[Stu77] Stutius, W. & Streifer, W., 1977. Silicon nitride films on silicon for optical waveguides. *Applied optics*, 16(12), pp.3218–22.

[Tag11] Taguchi, Y. et al., 2011. Statistical studies of photonic heterostructure nanocavities with an average Q factor of three million. *Optics express*, 19(12), pp.11916–21.

[Tho13] Thompson, J.D. et al., 2013. Coupling a single trapped atom to a nanoscale optical cavity. *Science (New York, N.Y.)*, 340(6137), p.1202.

[Thy12] Thyrrestrup, H. et al., 2012. Statistical Theory of a Quantum Emitter Strongly Coupled to Anderson-Localized Modes. *Physical Review Letters*, 108(11), p.113901.

[Top07] Topolancik, J. et al., 2007. Experimental Observation of Strong Photon Localization in Disordered Photonic Crystal Waveguides. *Physical Review Letters*, 99(25), p.253901.

[Vel06] Velha, P. et al., 2006. Ultra-high-reflectivity photonic-bandgap mirrors in a ridge SOI waveguide. *New Journal of Physics*, 8(9), pp.204–204.

[Vet10] Vetsch, E. et al., 2010. Optical interface created by laser-cooled atoms trapped in the evanescent field surrounding an optical nanofiber. *Physical Review Letters*, 104(20), pp.1–4.

[Vil94] Villeneuve, P.R. & Piché, M., 1994. Photonic bandgaps in periodic dielectric structures. *Progress in Quantum Electronics*, 18(2), pp.153–200.

[Vla99] Vlasov, Y. et al., 1999. Different regimes of light localization in a disordered photonic crystal. *Physical Review B*, 60(3), pp.1555–1562.

[Vyn12] Vynck, K. et al., 2012. Photon management in two-dimensional disordered media. *Nature Materials*, 11(12), pp.1017–1022.

[Wak05] Waks, E. & Vuckovic, J., 2005. Coupled mode theory for photonic crystal cavity-waveguide interaction. *Optics Express*, 13(13), p.5064.

[War07] Warken, F. et al., 2007. Ultra-sensitive surface absorption spectroscopy using sub-wavelength diameter optical fibers. *Optics Express*, 15(19), p.11952.

[Wea90] Weaver, R.L., 1990. Anderson localization of ultrasound. *Wave Motion*, 12(2), pp.129–142.

[Wei13] Wei Hsu, C. et al., 2013. Bloch surface eigenstates within the radiation continuum. *Light: Science & Applications*, 2(7), p.e84.

[Wie13] Wiersma, D.S., 2013. Disordered photonics. *Nature Photonics*, 7(3), pp.188–196.

[Wie97] Wiersma, D.S. et al., 1997. Localization of light in a disordered medium. , 390(6661), pp.671–673.

[Yab87] Yablonovitch, E., 1987. Inhibited Spontaneous Emission in Solid-State Physics and Electronics. *Physical Review Letters*, 58(20), pp.2059–2062.

[Yu14] Yu, S.-P. et al., 2014. Nanowire photonic crystal waveguides for single-atom trapping and strong light-matter interactions. *Applied Physics Letters*, 104(11), p.111103.

[Zan15] Zang, X. & Lalanne, P., 2015. Theoretical treatment of the interaction between two-level atoms and periodic waveguides. *arXiv:1506.01176*.

[Zho08] Zhou, L. et al., 2008. Controllable Scattering of a Single Photon inside a One-Dimensional Resonator Waveguide. *Physical Review Letters*, 101(10), p.100501.